

## OVERVIEW NO. 95

### CREEP RESISTANCE OF CMSX-3 NICKEL BASE SUPERALLOY SINGLE CRYSTALS

T. M. POLLOCK<sup>†</sup> and A. S. ARGON

Massachusetts Institute of Technology, Cambridge, MA 02139, U.S.A.

(Received 8 October 1990; in revised form 8 May 1991)

**Abstract**—Creep deformation in <001> oriented nickel base superalloy single crystals has been studied in an effort to assess the factors which contribute to the overall creep resistance of superalloys with high volume fractions of  $\gamma'$  phase. Detailed observations of three dimensional dislocation arrangements produced by creep have been made with the use of stereo electron microscopy. In the temperature range of 800–900°C at stresses of 552 MPa or lower, the dislocation-free  $\gamma'$  precipitates are resistant to shearing by dislocations. As a result, creep deformation occurs by forced bowing of dislocations through the narrow  $\gamma$  matrix channels on {111} planes. At moderate levels of temperature and stress there are incubation periods in virgin crystals prior to the onset of primary creep. The incubations arise because of the difficult process of filling the initially dislocation starved matrix material with creep dislocations from widely spaced sources. When the newly generated dislocations percolate through the cross section, incubation comes to an end and primary creep begins. In primary creep neither work hardening nor any type of recovery plays an important role. The creep rate decelerates because the favorable initial thermal misfit stresses between  $\gamma$  and  $\gamma'$  phases are relieved by creep flow. Continued creep leads to a build-up of a three-dimensional nodal network of dislocations. This three-dimensional network fills the  $\gamma$  matrix channels during steady state creep and achieves a quasi-stationary structure in time. *In situ* annealing experiments show that static recovery is ineffective at causing rearrangements in the three-dimensional network at temperatures of 850°C or lower. The kinematical dislocation replacement processes which maintain the quasi-stationary dislocation network structures during apparent steady state creep are not understood and require further study. Because of the impenetrability of the  $\gamma'$  precipitates, dislocations move through the  $\gamma$  matrix by forced Orowan bowing, and this accounts for a major component of the creep resistance. In addition, the frictional constraint of the coherent or semi-coherent precipitates leads to the build-up of pressure gradients in the microstructure, and this provides load carrying capacity. There is also a smaller component of solid solution strengthening. Work hardening is comparatively unimportant. Finite element analysis shows that the non-deforming precipitates are increasingly stressed as creep deformation accumulates in the matrix. In the later stages of steady state creep and during tertiary creep the stresses in the precipitates rise to high enough levels to cause shearing of the  $\gamma'$  particles by dislocations entering from the  $\gamma$  matrix. The recovery resistance of the material is in part due to a very low effective diffusion constant and in another part due to the fact that the three-dimensional dislocation networks formed in the  $\gamma$  matrix serve to neutralize the misfit between the  $\gamma$  and  $\gamma'$  phases.

**Résumé**—On étudie la déformation par fluage dans un superalliage monocristallin à base de nickel d'orientation <001>, dans le but d'estimer les facteurs qui contribuent à la résistance globale au fluage des superalliages contenant des fractions volumiques élevées de phase  $\gamma'$ . Des observations détaillées des arrangements tridimensionnels de dislocations produits par le fluage sont réalisées à l'aide de la microscopie électronique stéréo. Dans la gamme de 800 à 900°C, pour des contraintes de 552 MPa ou moins, les précipités  $\gamma'$  exempts de dislocations résistent au cisaillement par les dislocations. En conséquence, la déformation par fluage se produit par la courbure forcée des dislocations à travers les canaux étroits de matrice  $\gamma$  sur les plans {111}. Aux niveaux de températures et de contraintes modérés il existe, dans les cristaux vierges, des périodes d'incubation avant l'établissement du fluage primaire. Les incubations se produisent par suite de la difficulté qu'il y a à remplir la matrice, initialement vide de dislocations, par des dislocations de fluage provenant de sources largement espacées. Quant les dislocations nouvellement créées percolent par la section droite des canaux, l'incubation se termine et le fluage primaire commence. Au cours du fluage primaire, ni l'écrouissage, ni aucun type de restauration ne jouent de rôle important. La vitesse de fluage diminue, car les contraintes de désaccord thermique entre les phases  $\gamma$  et  $\gamma'$  initialement favorables sont dissipées par l'écoulement de fluage. Le fluage continu conduit à l'établissement d'un réseau de noeuds à trois dimensions. Ce réseau tridimensionnel remplit les canaux de la matrice  $\gamma$  pendant le fluage en régime permanent et réalise une structure quasi-stationnaire dans le temps. Des expériences de recuit *in situ* montrent que la restauration statique est inefficace pour réaliser des réarrangements dans le réseau tridimensionnel à 850°C ou à des températures inférieures. Les mécanismes cinématiques de remplacement de dislocations qui maintiennent le réseau de dislocations quasi-stationnaire pendant le fluage en régime permanent apparent ne sont pas compris et requièrent une étude ultérieure. À cause de l'impénétrabilité des précipités  $\gamma'$ , les dislocations se déplacent à travers la matrice  $\gamma$  par le mécanisme

<sup>†</sup>Present address: Department of Metallurgical Engineering and Materials Science, Carnegie-Mellon University, Pittsburgh, Pa., U.S.A.

de courbure forcée d'Orowan qui rend compte d'une composante majeure de la résistance au fluage. De plus, la contrainte de friction des précipités cohérents et semi-cohérents conduit à l'établissement de gradients de pression dans la microstructure et ceci fournit une capacité additionnelle de charge. Il existe aussi une plus petite composante due au durcissement de la solution solide. L'écrouissage est comparativement peu important. Une analyse par éléments finis montre que les précipités non déformés subissent une contrainte croissante lorsque la déformation par fluage s'accumule dans la matrice. Dans les derniers stades du fluage en régime permanent et pendant le fluage tertiaire, les contraintes dans les précipités s'élèvent à des niveaux assez élevés pour causer le cisaillement des particules  $\gamma'$  par les dislocations venant de la matrice  $\gamma$ . La résistance à la restauration du matériau est en partie due à la constante de diffusion efficace très basse et d'un autre côté au fait que le réseau tridimensionnel de dislocations formé dans la matrice  $\gamma$  sert à neutraliser le désaccord entre les phases  $\gamma$  et  $\gamma'$ .

**Zusammenfassung**—Die Kriechverformung von <001>-orientierten Einkristallen einer Superlegierung auf Nickelbasis wird untersucht, um die Ursachen des beobachteten Kriechwiderstandes von Superlegierungen mit einem hohen Volumanteil der  $\gamma'$ -Phase aufzufinden. Die während des Kriechens erzeugte dreidimensionale Versetzungsanordnung wird mittels Stereo-Elektronenmikroskopie analysiert. Im Temperaturbereich zwischen 800 und 900°C bei Spannungen von 552 MPa oder niedriger widerstehen die versetzungsfreien  $\gamma'$ -Ausscheidungen der Scherwirkung der Versetzungen. Dadurch läuft die Kriechverformung über das erwogene Ausbauchen der Versetzungen durch die engen Kanäle der Matrix auf {111}-Ebenen ab. Bei mäßigen Temperaturen und Spannungen treten Inkubationsperioden in dem unverformten Kristall vor dem Einsetzen des primären Kriechens auf. Diese entstehen wegen des schwierigen Prozesses, das anfangs versetzungsarme Matrixvolumen mit Kriechversetzungen aus den weit voneinander entfernten Quellen zu füllen. Wenn die neu erzeugten Versetzungen den Querschnitt durchlaufen können, ist die Inkubationsperiode beendet und das primäre Kriechen beginnt. In der Phase des primären Kriechens spielen weder Verfestigung noch Erholung eine wesentliche Rolle. Die Kriechrate sinkt, da die vorteilhaften anfänglichen thermischen Fehlpassungsspannungen zwischen  $\gamma$ - und  $\gamma'$ -Phase durch das Kriechen abgebaut werden. Weiteres Kriechen führt zum Aufbau eines dreidimensionalen Knoten-Netzwerks. Dieses füllt die Kanäle der  $\gamma$ -Matrix während des stationären Kriechens und führt zu einer in der Zeit quasi-stationären Struktur. *In-situ*-Ausheilexperimente zeigen, daß statische Erholung zu ineffektiv ist, um ein Rearrangement des dreidimensionalen Netzwerkes bei Temperaturen unterhalb von 850°C zu verursachen. Die kinematischen Versetzungs-Ersetzungsprozesse, welche die quasistationäre Struktur des Versetzungsnetzwerkes während des offenkundigen stationären Kriechens aufrechterhalten, sind noch nicht verstanden. Zusätzlich zur Nichtschneidbarkeit der  $\gamma'$ -Ausscheidungen als wesentliche Ursache des Kriechwiderstandes liefern Reibungseinflüsse durch kohärente oder semikohärente Ausscheidungen dadurch einen weiteren Beitrag, daß sich Druckgradienten in der Mikrostruktur aufbauen. Ein weiterer Beitrag röhrt von der Mischkristallhärtung her. Im Vergleich dazu ist die Verfestigung unwichtig. Die Analyse mit finiten Elementen zeigt, daß mit ansteigender Kriechverformung der Matrix die sich nicht verformenden Ausscheidungen immer stärker verspannt werden. In späteren Stadien des stationären Kriechens und während des tertiären Kriechens sind diese Spannungen in den Ausscheidungen so hoch, daß die  $\gamma'$ -Teilchen durch Versetzungen der Matrix geschnitten werden. Der Erholungswiderstand des Materials röhrt her von dem sehr niedrigen effektiven Diffusionskoeffizienten und von der Tatsache, daß das dreidimensionale Versetzungsnetzwerk in der  $\gamma$ -Matrix die Fehlpassung zwischen der  $\gamma$ - und der  $\gamma'$ -Phase kompensieren hilft.

## 1. INTRODUCTION

Nickel base superalloys have long been recognized as important engineering materials because of their excellent resistance to high temperature deformation. In particular, nickel base alloys in their single crystal form have been used widely in components such as turbine blades, where it is desirable to keep creep deformation to a minimum.

The general uniaxial creep response of <001> oriented nickel base single crystal alloys varies with the stress and temperature imposed, as well as the heat treatments which establish the final  $\gamma/\gamma'$  microstructure [1–7]. Primary creep transients have in some cases been reported to be absent [8], while under other conditions primary creep strains as high as 8% have been reported [9]. There may be a well established period of steady state creep [6], or a long period of

gradually accelerating tertiary creep may be observed [4]. "Incubation periods" following loading but prior to any measurable creep have also been observed in some cases [1, 3, 5, 10].

Since the creep resistance of these  $\gamma/\gamma'$  alloys is much higher than the creep resistance of either the  $\gamma$  or  $\gamma'$  materials in bulk form†, it is clear that the two phase microstructure is very important in building up the high levels of strength. However, there is no detailed understanding of why this occurs in the two phase material. An additional complicating factor is the fact that the aging heat treatments are performed in the same temperature range as the useful operating temperatures of these materials, leading to a somewhat unstable microstructure. This is especially true at temperatures in excess of 900°C where there is a dramatic rearrangement or "rafting" of the microstructure under the influence of an applied stress [6, 11].

Here we report the results of experiments aimed at identifying the sources of high temperature creep resistance in a two phase  $\gamma/\gamma'$  material with a

†The typical creep resistance of solid solution strengthened  $\gamma$  phase in bulk, at a strain rate of  $ca\ 5 \times 10^{-8}\ s^{-1}$ , at 850°C is 30–40 MPa [27], while that for the  $\gamma'$  phase under these same conditions is 40–50 MPa [28, 29].

high volume fraction of  $\gamma'$  phase. Observations were limited to the 800–900°C temperature range, where the precipitates are fairly stable in shape and distribution. Emphasis has been placed on understanding the creep response at small strains. An understanding of the details of the creep deformation process under these conditions can serve as a basis for approaching the more difficult problem of understanding creep deformation with unstable precipitates, as well as providing a framework for formulating physically realistic small strain constitutive equations.

In addition to the creep experiments and TEM observations we also present a number of analyses that discuss: (a) the mechanisms of penetration of  $\gamma$  phase dislocations into  $\gamma'$  particles; (b) the complex  $\gamma$  phase creep flow patterns between non-deforming  $\gamma'$  particles; and (c) the very low effective diffusion constants in the  $\gamma$  phase that explain part of its recovery resistance.

## 2. EXPERIMENTAL DETAILS ON MATERIALS AND PROCEDURES

The single crystal superalloy CMSX-3 was the subject of this experimental program. The nominal composition of this Mar-M-247 derivative alloy is listed in Table 1. The solution treatment given to the material consisted of 1293°C for 2 h plus 1298°C for 3 h in vacuum, followed by a gas fan cool. Figure 1 is a light micrograph of a solution treated crystal sectioned transverse to the growth direction. Remnants of the dendritic growth process are clearly visible. The dark etching lines in the interdendritic areas are associated with irregularly shaped  $\gamma'$  phase, which is just visible by light microscopy at high magnifications. Following machining, samples were given a two step aging heat treatment of 1080°C for 4 h, followed by 870°C for 20 h. This heat treatment produces cuboidal  $\gamma'$  particles which are on average 0.45  $\mu\text{m}$  in size along the cube edge. The volume fraction of  $\gamma'$  is about 0.70. Prior to testing, all samples were electropolished in a 20%  $\text{H}_2\text{SO}_4$  and methanol solution.

Samples for mechanical testing were machined from 16 mm diameter solid cylindrical bars, which were all within 7° of the  $\langle 001 \rangle$  orientation†. Button-head creep specimens measuring 61.9 mm in length with a cylindrical gauge section of 38.1 mm in length and 3.56 mm in diameter were used. Testing was done in a lever loading creep machine equipped with a vacuum furnace described in more detail elsewhere [12]. Loads were applied smoothly by initially supporting them with a hydraulic jack, and then slowly lowering the jack until the load was fully applied, in a time period of about 15 s. The furnace was equipped with tungsten heating elements, and temperatures

Table 1. Nominal chemical composition of CMSX-3

Element	Weight percent	Atomic percent
Cr	7.9	9.1
Co	4.6	4.7
Mo	0.5	0.3
W	8.0	2.6
Ti	1.0	1.1
Al	5.6	12.4
Ta	6.0	1.9
Hf	0.11	0.03
Ni	Bal.	Bal.

were monitored with thermocouples welded to the surface of the samples. The samples were mounted in slotted TZM grips. Strains were measured by four LVDTs mounted on a plate attached to the loading rod just outside the furnace. This was necessary due to the limited space inside the vacuum furnace. In this configuration, the LVDTs were approximately 10 cm away from the specimen. To be certain that no spurious strains were being measured, a sample which was identical to the test specimens, except with no reduction at the gauge section, was loaded under the usual test conditions, and showed negligible strains.

Stress-strain tests were performed in air in compression in a servo-hydraulic machine. Use of a logarithmic function generator allowed a constant true strain rate to be maintained, and also permitted a strain rate change at a pre-determined level of strain. The machine was equipped with a radiant heating furnace. Cylindrical specimens 5.1 mm in diameter and 7.6 mm in height were produced by centerless grinding and sectioning. A 4:1 mixture of 1990 glass and boron nitride powder was used for lubrication between the specimens and the TZM platens.

TEM specimens were prepared by conventional jet polishing in a solution of 10% perchloric acid, 9% distilled water, 13% butyl cellosolve, and 68% methanol. All TEM foils were taken from creep specimens which were cooled under load to preserve the dislocation arrangements. The foils were sectioned from planes transverse to the direction of

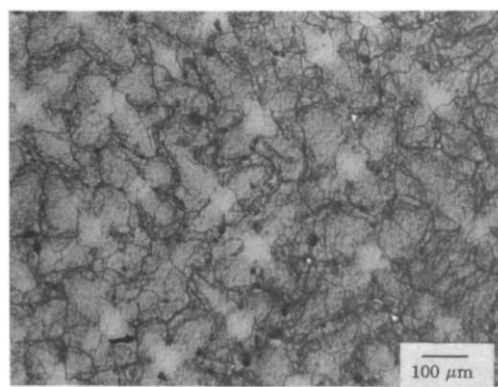


Fig. 1. Low magnification light optical micrograph of solution treated bar sectioned transverse to growth direction.

†We are grateful to Dr M. Döner of the Allison Gas Turbine Division of G. M. for supplying us with these single crystals.

the applied creep stress. Stereo-imaging techniques were used extensively to obtain a three-dimensional view of the dislocation arrangements.

*In situ* annealing observations were made with the use of a high temperature single tilt heating stage with a maximum temperature capability of 1300°C. For a more accurate estimate of the temperature of the foils during *in situ* annealing, the stage was calibrated by melting thin foils of Al, Ge, and Ag, whose melting points cover the temperature range of interest.

Measurement of changes of dislocation density as a result of the *in situ* annealing process were made by selecting an area for observation and recording a series of micrographs of the same area over a period of time. To calculate the total dislocation density, an image analyzer program was used to record lines in a micrograph, reduce them to a single pixel in width, and give a measurement of total line length. Foil thickness was estimated from a stereo pair, using the cube edges of the precipitates as a reference for measurement. The densities were then corrected to account for the dislocations that were invisible under the given diffraction conditions.

### 3. MECHANICAL TESTS

#### 3.1. Steady creep experiments

To establish creep stress exponents and activation energies, creep tests covering the temperature range of 800–900°C and stress range of 450–650 MPa were performed. In general the tests were not run to fracture; once the minimum creep rate was established, they were interrupted for the purpose of preserving the samples for microscopy. Within this limited range of experimental conditions, the creep curves of virgin samples show a brief primary transient followed by a period of minimum creep rate (which will for convenience be referred to as “steady state” creep), and a rather extended period of slowly accelerating tertiary creep. A representative curve at 850°C and 552 MPa is shown in Fig. 2. For the temperature range covered, the activation energy for creep determined by the usual procedure of comparing minimum creep rates at constant stress but increasing temperatures is 495 kJ/mol, and the creep stress exponent,  $n = \partial \ln \dot{\epsilon}_{ss} / \partial \ln \sigma$  is equal to 7.1.

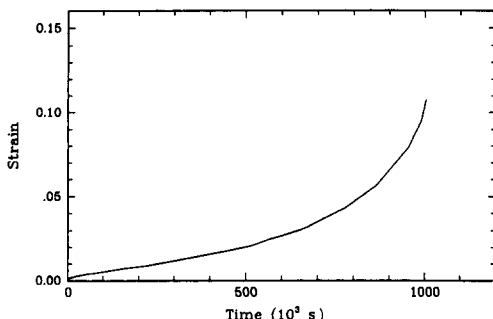


Fig. 2. Representative creep curve for <001> CMSX-3 at 850°C and 552 MPa. Fracture occurred at 273 h.

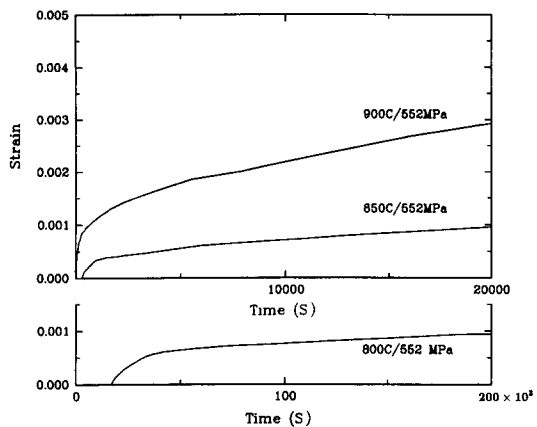


Fig. 3. Details of the incubation and primary creep behavior under 3 different conditions. Note the changed time scale for the 800°C data.

Figure 3 shows the early stages of the creep curves of virgin specimens at 552 MPa at the temperatures of 800, 850, and 900°C. (Note that there is a different time scale for the 800°C data.) There is no instantaneous plastic straining upon application of the stress. The elastic strains have been subtracted from this data. Close inspection of the curves shows incubation periods prior to the onset of the primary transient at 800 and 850°C. At 800°C the incubation period lasts for  $1.6 \times 10^4$  s, while at 850°C it is only about 600 s in duration, and at 900°C it is apparently immeasurably short. For a constant stress, the incubation period increases in length with decreasing temperature, and similarly, for a constant temperature, a lower stress will lead to a longer incubation time. From this data an activation energy of 658 kJ/mol is obtained for the incubation process. At 850°C the length of the incubation period showed some scatter from sample to sample. Also, because of the very small strains being measured, it is difficult to establish the exact shape of the strain–time curve in the transition from the incubation to the primary transient.

#### 3.2. Non-steady creep experiments

To determine the effect of static recovery on the mechanical response of the material in the creep regime, a sample was loaded and allowed to creep until the steady creep rate was established at 850°C–552 MPa. The sample was then unloaded by 90% and permitted to rest at 850°C for varying amounts of time. Following the rest, the sample was reloaded back to 552 MPa for observation of the reloading transients. Successive rest periods of 180,  $1.8 \times 10^3$ ,  $1.62 \times 10^4$ , and  $1.62 \times 10^5$  s all gave similar results with respect to the reloading transient. In Fig. 4 the results for the sample annealed for  $1.62 \times 10^4$  s (4.5 h) are plotted. The reloading transient is very slight and the strain accumulated in this transient is less than 10% of the strain accumulated during the initial primary transient.

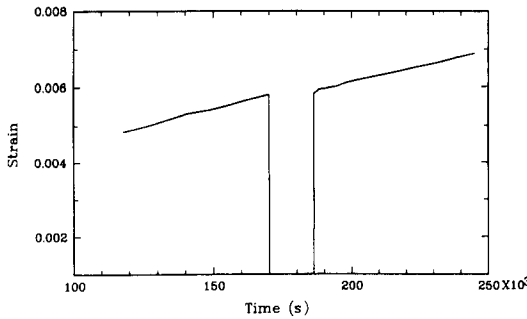


Fig. 4. Results of a recovery test, where a sample was unloaded during creep for  $1.6 \times 10^4$  s (4.5 h). Only a slight transient is present upon reloading at temperature (850°C at 552 MPa).

Stress jump and drop tests were conducted at 850°C on a sample which was initially creeping at a steady rate at 552 MPa. Starting with 0.87% accumulated creep strain, Figs 5(a) and 5(b) show the results of a stress jump from 552 to 607 MPa and the following drop from 607 MPa back to 552 MPa. Upon increasing the load, there is an instantaneous elastic extension followed by a brief transient lasting about 300 s, and a new steady state creep rate is quickly established. Using the new steady state creep rate, a steady state creep stress exponent of  $n = 7.3$  is obtained. Unloading back to 552 MPa, the original creep rate at 552 MPa is re-established after a period of zero creep which lasts for 535 s. These transients are brief compared to the initial primary transient.

### 3.3. Stress-strain experiments

In order to probe the material behavior under different loading conditions, constant true strain

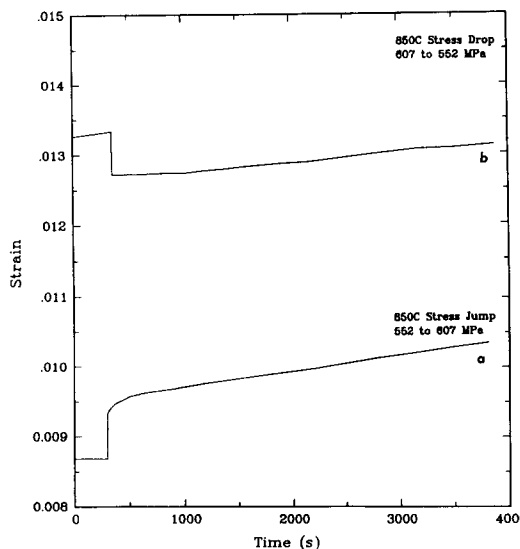


Fig. 5. (a) Results of a stress jump from 552 to 607 MPa after accumulation of 0.87% strain at 850°C and 552 MPa. Instantaneous elastic extension is followed by a brief transient of decelerating creep rate. (b) A subsequent stress drop from 607 to 552 MPa, where there is an elastic contraction and a period of zero externally measurable creep which lasts for 535 s.

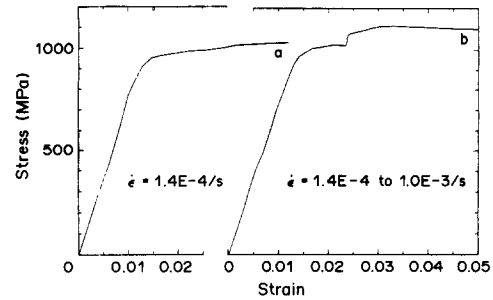


Fig. 6. (a) Stress-strain curve for CMSX-3 at 800°C tested in compression at a rate of  $1.4 \times 10^{-4}$ /s. (b) Strain rate jump during compression at 800°C.

rate and strain rate jump experiments were performed. The results for compression of a sample at a constant strain rate of  $1.4 \times 10^{-4}$ /s at 800°C are shown in Fig. 6(a). At this imposed rate, the 0.2% offset yield strength is 950 MPa, which is approximately twice the magnitude of the stresses imposed during the creep tests. Note also that the flow stress continues to rise during the test.

In Fig. 6(b) are the results for a strain rate jump to  $1 \times 10^{-3}$ /s after approximately 2% deformation at  $1.4 \times 10^{-4}$ /s. From this and other such jumps a stress exponent can again be calculated and is  $n = 36.2$ . This is a very high exponent, compared to the steady state creep exponent of 7.1 and indicates that deformation in this range of strain rates has the characteristics of thermally activated glide rather than diffusion controlled creep. For a strain rate jump from  $1.4 \times 10^{-4}$ /s to  $1 \times 10^{-2}$ /s the stress exponent is  $n = 38.7$ .

## 4. TRANSMISSION ELECTRON MICROSCOPY

### 4.1. The aged material

Figure 7(a) is a micrograph of the  $\gamma/\gamma'$  structure in the aged condition. The cuboidal  $\gamma'$  precipitates are coherent with the matrix with only isolated dislocations at the interfaces. The micrograph in Fig. 7(a) is representative of the structure over very large regions in the aged material. However, as shown in Fig. 7(b), regions of "grown in" dislocations associated with irregularly shaped  $\gamma'$  were occasionally seen in the aged material. These areas are widely spaced and appear to be associated with the darkly etched "lines" noted in Fig. 1. These "linear" tangles of grown-in dislocations all lie in the matrix material and have the same Burgers vector. The local density of these grown-in dislocations is estimated from the micrographs to be about  $10^7/\text{cm}^2$ . No dislocations have been observed inside the  $\gamma'$  in the aged material.

### 4.2. The incubation period

The following observations were made on samples taken from a specimen which was tested at 825°C/450 MPa, where an incubation period of the order of hours is expected. The test was interrupted

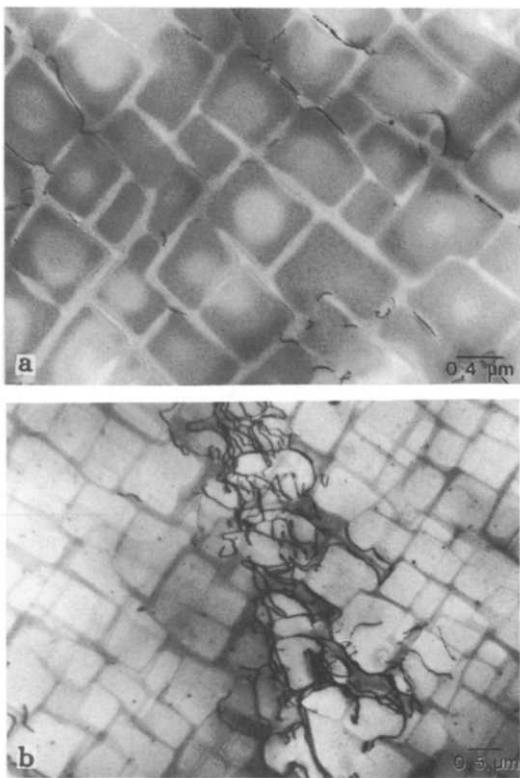


Fig. 7. (a) TEM micrograph of aged microstructure of CMSX-3 with cuboidal  $\gamma'$  and occasional dislocations at the  $\gamma/\gamma'$  interfaces. (b) TEM micrograph of aged microstructure of CMSX-3. Occasional networks of "grown-in" dislocations contained in the matrix are present, as shown at the center.

and the specimen cooled under load after only 2 min of straining. No externally measurable strain was accumulated within this time, within the resolution of strain measurement, which was  $3 \times 10^{-5}$ .

Over very large areas, the incubation samples resembled the aged samples, showing many coherent cuboidal precipitates with only isolated dislocations present. However, the incubation samples differed from the aged samples in the regions where the prior "grown-in" dislocations were present. During the incubation period the grown-in dislocations serve as sources, and creep dislocations spread from these areas into the previously dislocation free areas. In Fig. 8 the grown-in network of dislocations is at the center of the micrograph, and the longer, more straight dislocations are bowing out and spreading from the center to the left and right. Stereo imaging has established that all of these dislocations are in the  $\gamma$  matrix channels and as a result of their confinement to the matrix passages, the expanding loops assume very long, narrow shapes. Figure 9 shows several clear examples of dislocations spreading out into previously dislocation free areas. Even in the thin foil, a single loop, such as the one marked "A", can be traced across many precipitate dimensions. This loop is contained in a matrix passage parallel to the foil plane, which itself was normal to the direction of

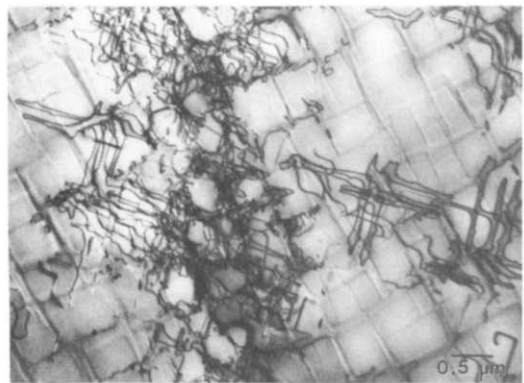


Fig. 8. Dislocations spreading from the grown-in dislocation network during the incubation period. The prior network of grown-in dislocations serves as a source of dislocations, and loops spread from the center network outward.

the applied tensile stress. Several leading segments of pure screw orientation of the loops that are bowing out, are marked by arrows in Fig. 9. Stereo pairs show that very few of these leading screw segments are held up at the  $\gamma/\gamma'$  interfaces. Instead they have been captured in the process of slowly moving through the matrix gaps, apparently against a solid solution resistance.

A higher magnification view of the bowing dislocations is shown in Fig. 10. Near the area marked "B" there are several dislocation loops which appear to have taken a  $90^\circ$  change in direction during the process of traveling through the matrix. Stereo pairs show that these right angle turns in the dislocations ( $\mathbf{b} = a/2[0\bar{1}1]$ ) must have resulted from the cross gliding of the leading screw dislocation segments from the  $(\bar{1}11)$  plane to the  $(111)$  plane. (The  $[001]$  is normal to plane of the micrograph.) In this case the leading screw segments have traveled from "A" to "C", leaving  $60^\circ$  mixed dislocations at the interfaces of the  $\gamma'$  particles, and cross-glide has occurred at "B". Such cross glide events were frequently observed in the samples, and are necessary for the systematic spreading of the dislocations into the

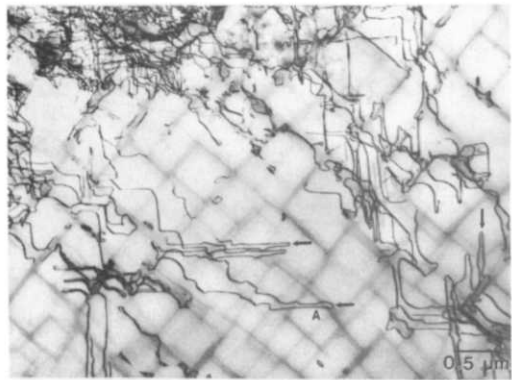


Fig. 9. Long, narrow dislocation loops spreading through the matrix during the incubation period. These dislocations originated from the network in the upper left corner. Arrows denote the leading screw components of the loops.

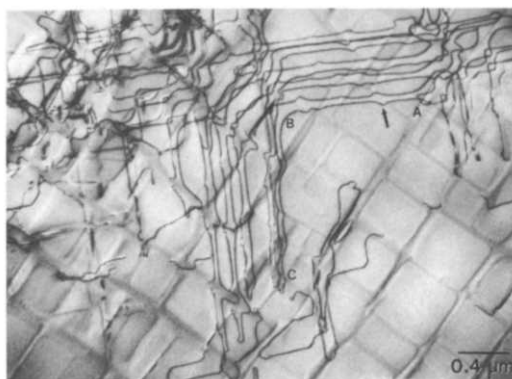


Fig. 10. Modes of dislocation filling of the material during the incubation period. At B, the dislocations cross-glide as they spread from A to C. The arrow indicates a portion of a loop which is bowing into a matrix channel normal to the one containing the long, narrow loop.

narrow  $\gamma$  channels from a limited number of sources. Another mode of dislocation spreading is marked by the arrow in Fig. 10. As a loop expands through a horizontal  $\gamma$  matrix channel (contained in the plane of the foil), many vertical matrix channels are also encountered, and the dislocations attempt to spread into these vertical channels. At the arrow a dislocation is shown beginning to expand into the vertical channel. This gives rise to periodic bulges on the otherwise straight dislocation lines contained in the matrix channels in the plane of the foil. The relatively large  $\gamma'$  precipitates and the highly restricted motion of the dislocations through the narrow matrix channels generally prevent the formation of Orowan loops around the precipitates.

#### 4.3. Primary creep

During primary creep the material continues to fill with dislocations. All creep deformation continues to be accomplished by bowing the dislocations through the matrix channels on  $\{111\}$  planes. Figure 11(a) and (b) are representative of the dislocation structure after 35 min ( $\epsilon = 4.6 \times 10^{-4}$ ) and 402 min ( $\epsilon = 0.001$ ),

respectively at 850°C and 552 MPa. In Fig. 11(a) nearly all of the dislocations have the same Burgers vector, and many of the matrix passages are still free of dislocations. In comparison, Fig. 11(b) shows a higher density of dislocations, with nearly all of the matrix channels containing some dislocations. Later in primary creep multiple dislocations with  $a/2\langle 110 \rangle$  Burgers vectors are present locally in a single matrix channel. Two sets of dislocations from different sources have apparently penetrated into a single channel in Fig. 12(a) and (b), leading to reactions between the different dislocations.

Figure 13 is a stereo pair of the dislocation structure in primary creep that is typical of the many such pairs that have been routinely studied. The figure clearly demonstrates the characteristic three-dimensional arrangement of the dislocations in a narrow  $\gamma$  channel in primary creep. Near the area marked "A" the cuboidal precipitates with light appearance extend through the thickness of the foil. In the through-the-thickness matrix passage to the left of "A" the dislocations are bowing through the gap vertically, as shown schematically in Fig. 14(a). Again referring to Fig. 13, the long, straight dislocations near area "B" are contained in a single horizontal channel spanning across a number of  $\gamma'$  particles, as shown in Fig. 14(b). These dislocations lie at an angle of 45° to the cube face at the  $\gamma'$  interfaces as a result of multiple loops bowing through the channels on  $\{111\}$  planes. They are mixed in character, with their Burgers vectors inclined at an angle of 60° to the dislocation line. As a consequence, these dislocations are at least partially relieving the misfit on the horizontal faces during primary creep.

The dislocations which are contained in the vertical channels (parallel to the direction of applied stress, and normal to the plane of the foil, as near "A") are also usually mixed in character, although pure screw dislocations are sometimes found in the vertical interfaces which contain the Burgers vector of the dislocation at the interface. Considering the geometry of the microstructure, it is not possible to completely

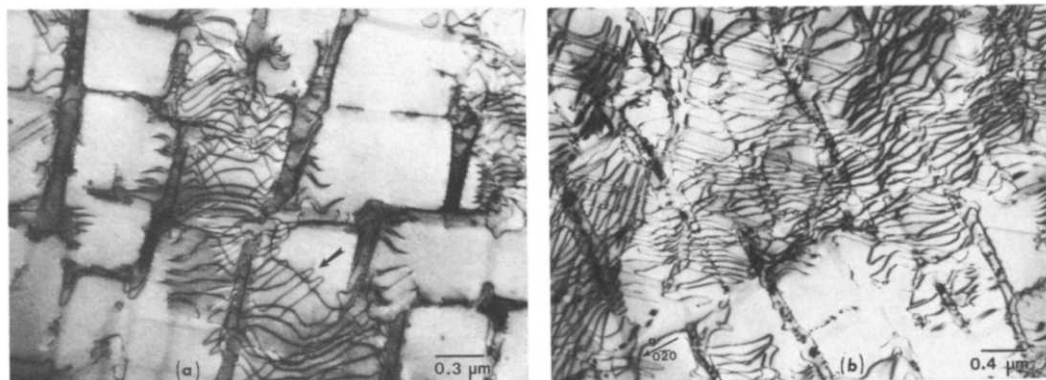


Fig. 11. (a) Dislocation distribution in the early stages of primary creep. Some matrix regions are still free of dislocations, and spreading continues by bowing dislocations through the matrix, as shown in the area marked by the arrow. (b) Typical dislocation distribution in the latter stages of primary creep. The density of dislocations has increased and few channels are left unpopulated.

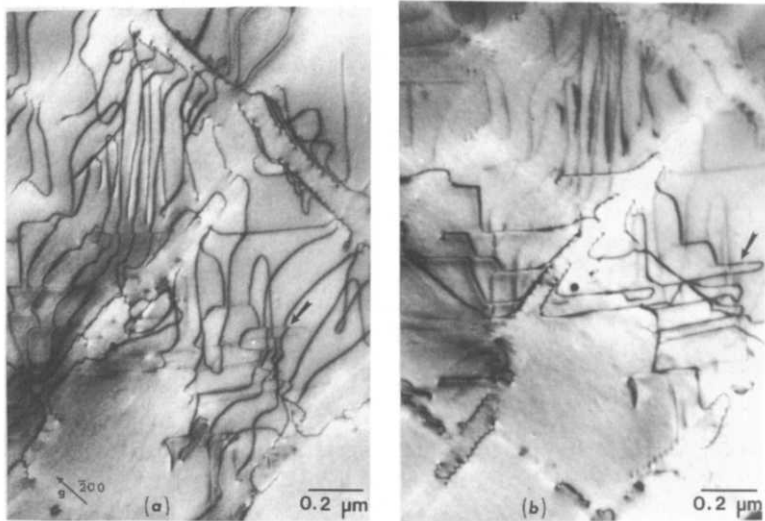


Fig. 12. In the later stages of primary creep, dislocations from widely spaced sources begin to interpenetrate and react. Two sets of dislocations (one set only visible by residual contrast) are present in the matrix channel marked by the arrow.

relieve the misfit by depositing creep dislocations of edge character, by glide motion, on the interfaces during the bowing out process. However, with the operation of multiple slip systems the misfit may be relieved by building up a series of dislocations of mixed character at the interfaces. The issue of the relief of the misfit will be discussed below.

The mode of bowing of screw dislocations through narrow matrix channels (discussed earlier [13-15]), and deformation confined to the matrix material in

the early stages of creep has been noted by Caron, Khan and co-workers [3, 16] in CMSX-2 at 760° and 850°C as well as by Fredholm and Strudel [17] in a high Ta experimental alloy tested at 1050°C. More recently, bowing out of screw dislocations accompanied by cross glide events has been reported during primary creep at 760°C in NASAIR 100 [18] and 980°C in SRR99 crystals [19]. This general tendency for deformation to occur in the narrow matrix channels in nickel base single crystals in the

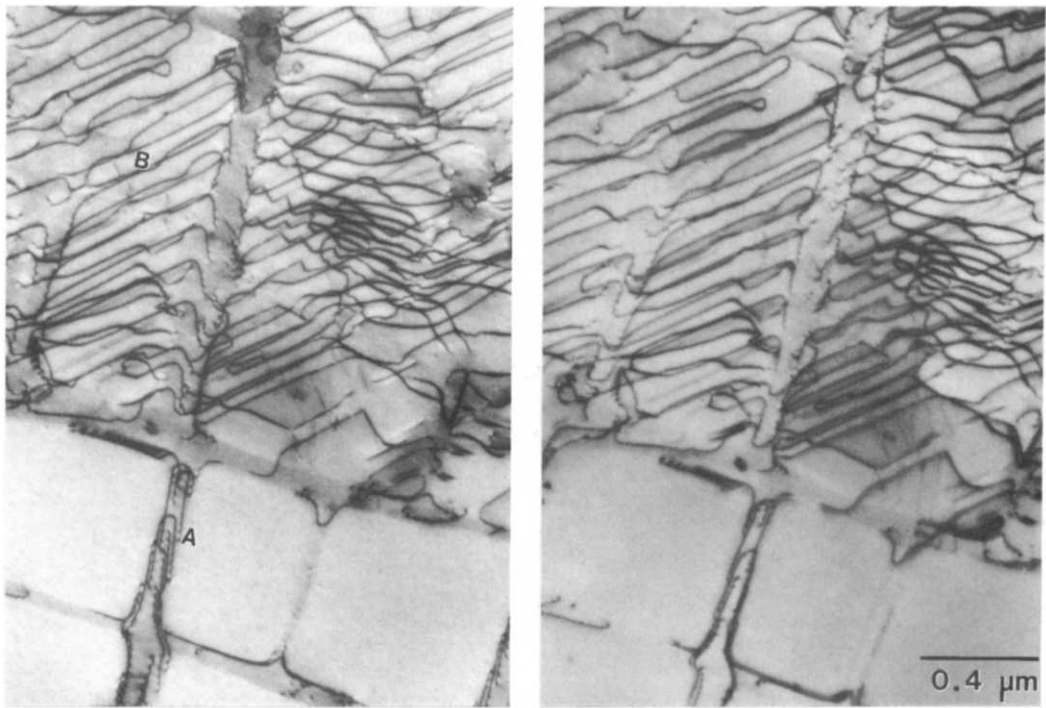


Fig. 13. Stereo pair of dislocation structure during primary creep. Dislocations to the left of (A) are in a vertical matrix channel. The precipitate at A extends through the foil thickness. The dislocations in region B are in a horizontal matrix channel which is contained in the plane of the foil.

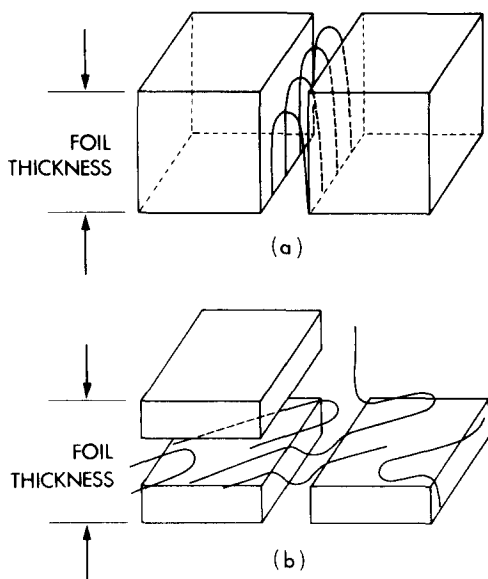


Fig. 14. Schematic of dislocation arrangements. Dislocations are bowing out through a vertical channel in (a). In (b) the dislocations are bowing through a horizontal channel, leaving long narrow loops in the plane of the foil.

early stages of creep will be shown to be related to the high levels of misfit stresses present in the matrix due to the coherent precipitates.

#### 4.4. Steady state creep

Once the "steady state" creep regime is reached the  $\gamma$  matrix has become completely filled with dislocations, with no matrix channels left unpopulated. Figure 15 shows a low magnification stereo pair of the dislocation structure after creep at

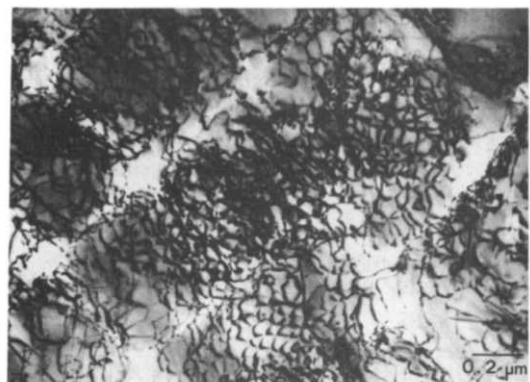


Fig. 16. Matrix dislocation networks during steady state creep. A very organized three-dimensional nodal network is present locally, and many of the dislocations are associated with the  $\gamma/\gamma'$  interface.

$850^{\circ}\text{C}/552 \text{ MPa}$ , giving 2.34% strain. Multiple slip systems have been activated during steady state creep and as a result a three-dimensional nodal network has built up in the matrix. A significant fraction of the dislocations present in the network form a "cage" around the  $\gamma'$  precipitates. The interfaces of the  $\gamma'$  particles are now not as sharply defined along  $\{001\}$  planes as was the case in the early stages of the creep process. There are very few dislocations present which are not associated with the three dimensional network. Figure 16 shows the network in a  $\gamma$  channel in more detail. It can be seen that in some areas the network is more organized with a large number of the dislocations associated with the interface, such as at the center of Fig. 16. In other areas the matrix dislocation density was much higher, with more dislocations

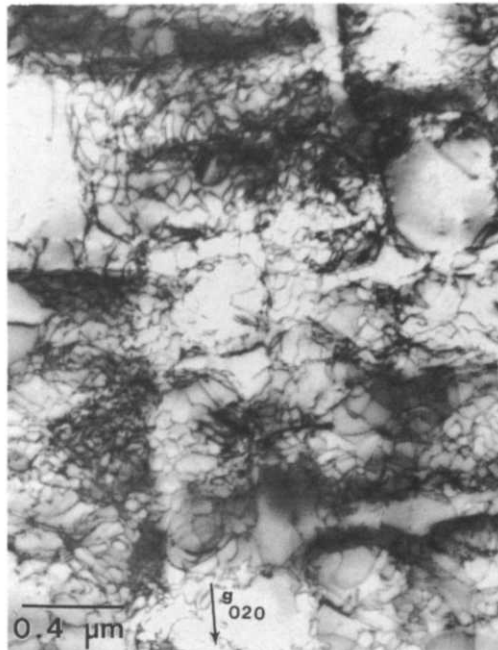


Fig. 15. Stereo pair of the steady state dislocation structure showing all of the dislocations residing in the matrix material.

filling the matrix space. Once steady state was achieved there were no readily noticeable differences in dislocation density for samples which accumulated different amounts of creep strain; apparently a quasi-stationary dislocation structure was attained. Viewing the networks by stereo imaging, it could be seen that the spacing of dislocations in the network was in the range of 50–120 nm, with 60–80 nm being the most commonly observed separation, characteristic of steady state, at 850°C/552 MPa. Since the dislocations are present as a result of the creep process, and the network is three-dimensional in nature, there are local variations in the organization of the dislocations. Burgers vector analyses on selected local areas of the networks showed them to be composed of three sets of dislocations, which are generally mixed in character. The networks lie in {111} planes and the Burgers vectors of the three sets of dislocations are the three coplanar  $a/2\langle 011 \rangle$  type dislocations. However, only local areas of the network lie in a single plane. Dislocations with Burgers vectors of  $a/2[110]$  and  $a/2[\bar{1}10]$  are less frequently observed than the other  $a/2\langle 011 \rangle$  types. These networks composed of  $a/2\langle 110 \rangle$  slipping dislocations and reaction products are a common characteristic of steady state creep in nickel base alloys [2, 3, 19, 20].

During the later stages of steady state creep the  $\gamma'$  precipitates are occasionally sheared. Figure 17 shows pairs of dislocations shearing through a precipitate on a {111} plane late in steady state creep ( $\epsilon > 2.2\%$ ). These shearing events are more common as creep strain is accumulated in the matrix in the tertiary stage and apparently related to the stresses in the  $\gamma'$  particles that increase steadily (see Section 6 below). A micrograph from a sample which was tested to fracture at 850°C/552 MPa (273 h) is shown in Fig. 18. Viewing this region in stereo, it could be seen that all of the isolated dislocations in the light areas are now lying inside the  $\gamma'$  precipitates. The precipitates have now also coarsened to some extent, and in many areas they are extending through the thickness of the foil.



Fig. 17. A precipitate sheared by dislocations in the later stages of steady state creep.

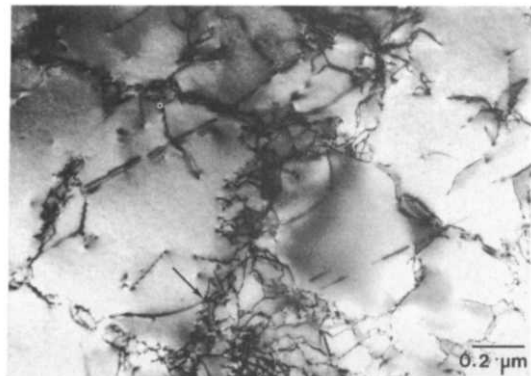


Fig. 18. Dislocations in a  $\gamma'$  precipitate in a sample tested to fracture at 850°C. In the light areas the precipitates extend through the thickness of the foil and all the isolated dislocations in these areas are in the  $\gamma'$  phase.

#### 4.5. Recovered dislocation structures

In Fig. 19 the dislocation structure is shown after 750 h ( $2.7 \times 10^6$  s) of bulk static annealing at 850°C. This annealing treatment was given to a sample which was first crept to steady state at 850°C/552 MPa and then cooled under load. Clearly, the networks have persisted even after extended periods of annealing. Stereo pairs showed, however, that the recovered network is now more organized and has coarsened to some degree relative to the original steady state network, with dislocation spacings being in the range of 80–100 nm. Compared to the steady state three-dimensional network, the recovered network is associated with the  $\gamma/\gamma'$  interfaces to a greater degree than before. A Burgers vector analysis showed that locally the network is composed of dislocations with three different  $a/2\langle 110 \rangle$  Burgers vectors, two of which are associated with active slip systems, and the other set, apparently being a reaction product.

#### 4.6. Dislocation structures following compression testing

Figure 20 shows the dislocation arrangements following constant true strain rate compression testing at 800°C at a rate of  $\dot{\epsilon} = 1.4 \times 10^{-4}/\text{s}$ . After 4.5%

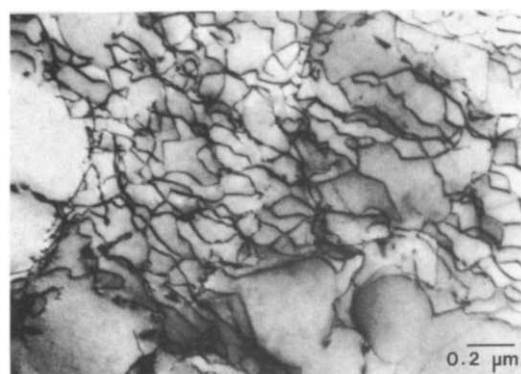


Fig. 19. Recovered dislocation networks in the matrix after 750 h of bulk static annealing at 850°C. The dislocations are largely associated with the  $\gamma/\gamma'$  interfaces.

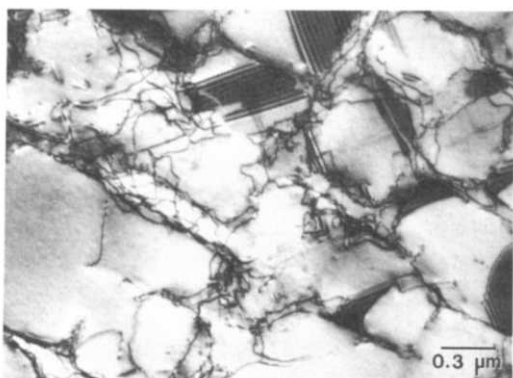


Fig. 20. Shearing of the  $\gamma'$  precipitates as a result of compression at a rate of  $1.1 \times 10^{-4}$ /s at  $800^\circ\text{C}$ . Stacking faults which extend across the precipitate are present on multiple  $\{111\}$  planes.

strain the sample was unloaded and quenched within 3 s. The maximum stress recorded during the compression test was 1024 MPa. Under these rather high stresses the precipitates are easily sheared by dislocations, and isolated pairs of dislocations as well as stacking faults are observed inside the  $\gamma'$  precipitates. The stacking faults are present on multiple  $\{111\}$  planes. The structure indicates a mode of deformation quite different from that observed as a result of the slower creep deformation at lower stresses. Clearly, data from stress-strain tests at these relatively high rates is not useful in developing a mechanistic understanding of the creep response, as we will elaborate below.

#### 4.7. In situ annealing observations

Foils from samples which were pre-deformed to steady state were prepared to observe any dislocation rearrangement during *in situ* annealing. The observations were made at temperatures around  $850^\circ\text{C}$  since this was the temperature of interest in the creep experiments. At temperatures above  $900^\circ\text{C}$  it was difficult to make observations, since fairly rapid degradation of the sample surfaces occurred. Annealing experiments on six different samples were completed at temperatures near  $850^\circ\text{C}$ , with no significant differences noted from sample to sample. The area of observation was always a horizontal matrix channel contained in the plane of the foil. In one sample the matrix channel was enclosed by precipitates on both sides. It is interesting to note that the behavior of this sample was not different from the others where the matrix material was not isolated from the foil surface by precipitates. This is a direct consequence of a rather substantial solid solution resistance to dislocation motion, as will be discussed below.

Figure 21 shows a series of micrographs where the sample was initially heated to  $845^\circ\text{C}$  for 45 min and subsequently the temperature was increased to  $882^\circ\text{C}$  and held. A comparison of the structure at the start, in Fig. 21(a), and after 17 min at  $845^\circ\text{C}$ , in Fig. 21(b), showed very little change in the dislocation arrange-

ments. The changes which did occur in the dislocation structure took place on a very local scale of the order of the network spacing, such as in the area identified by arrows in the photographs. The changes were fairly smooth, and usually difficult to discern in real time. Occasionally some motion was observed for a single dislocation which glided a short distance and annihilated or left through the foil surface, but this was a rare event. There was no general collapse of the three dimensional network and no static recovery with the jerky type motions seen by Prinz *et al.* [21] in pure single phase metals such as nickel and copper. Figure 21(c) shows the network after a temperature increase to  $882^\circ\text{C}$  for 31 min. Now there are noticeable changes in the three-dimensional matrix network. The overall density of dislocations

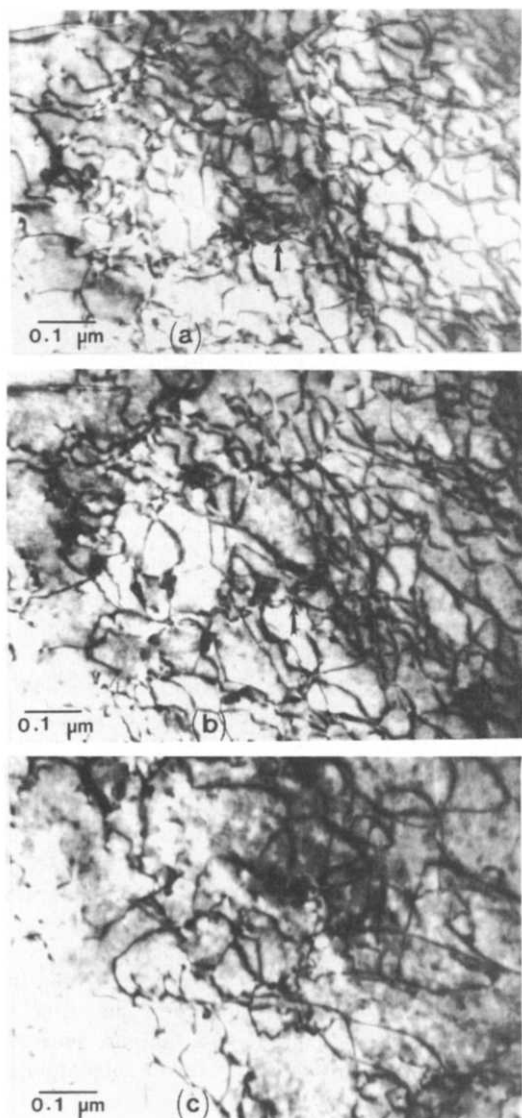


Fig. 21. Dislocation structure at the start of the  $845^\circ\text{C}$  *in situ* annealing experiment (a). Dislocation structure after 17 min at  $845^\circ\text{C}$ , showing only local rearrangements (b). Dislocation arrangements after 45 min at  $845^\circ\text{C}$  and 31 min at  $882^\circ\text{C}$  (c).

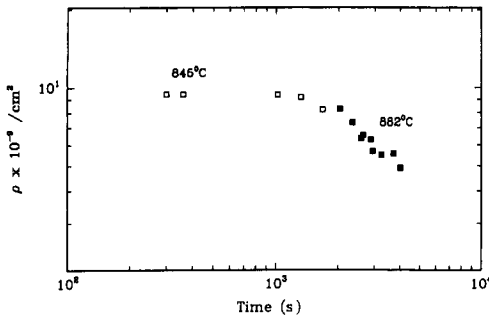


Fig. 22. Dislocation densities during the 845 and 882°C *in situ* annealing experiment.

(still confined to the  $\gamma$  channels) has decreased and the network has become quite coarse. Again the changes were not due to a jerky collapse of the network, but to a more gradual and quasi-viscous coarsening. From the series of micrographs obtained in this experiment, changes in dislocation density were measured and are plotted in Fig. 22. From this it can be seen that there were no important changes in dislocation density at 845°C, but at 882°C there were measurable changes as a result of the static annealing process. A straight line of slope of  $-0.74$  can be fitted to the 882°C data, and from this the rate of decrease of dislocation density was found to be proportional to the density as  $d\rho/dt \propto \rho^{2.3}$ .

## 5. MECHANISMS OF RESISTANCE TO DISLOCATION MOTION

### 5.1. The initial microstructure and the incubation period

An interesting aspect of the creep deformation of the nickel base superalloy single crystals discussed here is the "incubation" process which precedes the primary creep transient at moderate levels of temperature and stress. The micrographs of the material in the aged condition clearly show that the initial microstructure contains very few dislocations. Stereo pairs of dislocation structures during the incubation confirm that the  $\gamma'$  precipitates are effective barriers to dislocations. As a result, spreading dislocations through the matrix material is a difficult process, which requires bowing of the dislocations through the narrow matrix channels. Before macroscopic creep deformation can be detected, dislocations must percolate through the cross-section of the sample at least in a few places. The dislocation structures that are found, following straining at 825°C and 450 MPa for 120 s (Figs 8–10) clearly show that the deformation has not progressed this far, since the creep dislocations are present in only a small fraction of the area, immediately adjacent to the grown-in networks. If the applied stress and temperature are low enough, then the time for this initial filling process may be quite long, giving extended periods of no externally measurable creep strain (within the resolution of strain measurement), while elastic strain

is converted into creep strain only in isolated local regions.

### 5.2. Orowan resistance to dislocation motion

Before the dislocations can be forced through the matrix channels, the applied stresses must be high enough to overcome the local Orowan resistance of the channels, which is simply

$$\tau_{or} = \frac{\mu b}{l} = \sqrt{\frac{2\mu b}{3h}} \quad (1)$$

where  $\mu$  is the shear modulus,  $b$  the Burgers vector, and  $l$  is the channel dimension along the  $\langle 110 \rangle$  direction across a channel of thickness  $h$ . With an average matrix channel thickness of

$$h = 60 \text{ nm}, \quad l = 60\sqrt{3/2} = 73.5 \text{ nm},$$

$$b = 0.254 \text{ nm}, \quad \text{and} \quad \mu = 48.2 \text{ GPa}.$$

This gives an Orowan resistance of 166 MPa which we will take as typical for further analysis below. Dividing by the appropriate Schmid factor, a uniaxial applied stress of 408 MPa is required for just bowing dislocations through the typical matrix channel.

### 5.3. Misfit stresses

In addition to the Orowan resistance, it is also necessary to consider the misfit stresses—at least for the initial phases of the deformation before they are relieved. It is difficult to accurately determine the level of misfit at high temperatures. The  $\gamma/\gamma'$  misfit is temperature dependent due to the differing coefficients of thermal expansion of the two phases. After annealing for long periods at 1050°C, Fredholm and Strudel [17] determined a misfit of  $-0.33\%$  ( $a_m > a_p$ ) in CMSX-2 by measuring dislocation spacings at the interfaces. Since the driving force to relieve misfit falls quickly as dislocations begin to accumulate at the interfaces, as we will demonstrate in Section 6, the misfit is likely to be largely but not completely relieved by high temperature annealing. High temperature X-ray diffraction measurements by Nathal *et al.* [22] gave a misfit of about  $-0.19\%$  at 850°C for an alloy somewhat similar to CMSX-3. With the available information on coefficients of thermal expansion [23, 24] a misfit of  $-0.305\%$  is estimated at 850°C for CMSX-3. Since the precipitates are coherent, this misfit produces biaxial compressive misfit stresses of 433 MPa in the matrix parallel to the planes of the interfaces, and a 50 MPa tensile stress normal to the interfaces [25]. The magnitudes of the stresses have been obtained in a finite element study of the thermal misfit at 850°C in CMSX-3 and are discussed further in Section 6 below. With the application of a uniaxial stress in the range of 450–552 MPa, one component of misfit in the vertical matrix channel (parallel to the applied stress) is completely neutralized, while in the channel normal to the applied stress, the latter adds to the misfit stresses present. This leads to very high

Table 2. Incubation times for initiation of creep deformation and related driving stress

Applied tensile stress (MPa)	Total resolved misfit stress (MPa)	Total resolved stress (MPa)	Temperature (K)	$t_i$ , Incub. time (s)
552	178	403	1073	$1.59 \times 10^4$
450	189	373	1123	$4.50 \times 10^3$
552	189	415	1123	$6.00 \times 10^2$

equivalent stresses in the horizontal channels as creep begins. With an applied stress of 450 MPa (the same stress applied to the sample from which the incubation micrographs were taken), the equivalent stress in the vertical channels is 468 MPa, while in the horizontal channels it is 934 MPa. Therefore, it is expected that the dislocations would move in the horizontal matrix channels far more easily than in the vertical channels. In the incubation micrographs (Figs 8–10) this is found to be the case. The horizontal matrix channels lie in the plane of the micrographs, and the long, narrow loops are contained in the horizontal channels. Looking closely, it is clear that very few dislocations are threading vertically through the foil. In addition, the dislocations which show a tendency to spread into the vertical channels that are encountered as a loop moves through a horizontal channel (producing "bumps" on the otherwise straight lines) have traveled only a short distance into the vertical channels relative to the motion of the leading segment in the horizontal channel.

#### 5.4. Solid solution resistance

Finally, viewing the incubation micrographs in stereo, it also appears that during the incubation period, the dislocations move through the channels in a somewhat viscous manner. Very few of the segments that are bowing out are held up at the interfaces; instead they have been captured in the state of slowly moving along through the matrix. This is taken as evidence that in this heavily alloyed matrix material there are substantial solid solution drag forces acting on the dislocations as they move through the  $\gamma$  channels. Rarely do the dislocations spread in a manner which produces a simple Orowan loop around a single precipitate.

From fundamental considerations [26] we take the form of the solid-solution-resistance-governed-velocity of dislocations (screw segments) to be

$$v = v_0 \exp \left[ -\frac{Q - (\tau - \tau_{or})V^*}{kT} \right] \quad (2)$$

where  $v_0$  is a pre-exponential factor relatively independent of both stress and temperature,  $Q$  is the asymptotic activation free energy for dislocation

†The misfit stresses in the  $\gamma$  channels are, of course, not uniform but vary somewhat between the center of a  $\gamma'$  face to the edges. The finite element study of the stresses in the  $\gamma$  channels discussed in Section 6 and referred to above has indicated that these variations amount to a 4% reduction of the average resolved stress below the peak value occurring at the center of the face (Appendix I). This has been taken into account here.

motion at vanishing stress, and  $V^*$  is an activation volume. Furthermore,  $\tau$  is the resolved shear stress on the {111} plane in the active <110> direction for the specific slip systems, and  $\tau_{or}$  is the Orowan resistance of the narrow  $\gamma$  channels which will be taken as 166 MPa as estimated above. For the horizontal  $\gamma$  channels transverse to the applied tensile stress in the  $\bar{3}$  direction, the resolved shear stress is

$$\tau = (\sigma_{3a} + \sigma_{3t} - \sigma_{1t})(1/\sqrt{6}) \quad (3)$$

where  $\sigma_{3a}$  is the applied tensile stress,  $\sigma_{3t}$  is the tensile misfit stress acting across the horizontal  $\gamma$  channel and  $-\sigma_{1t}$  is the biaxial compressive misfit stress acting in the plane of the  $\gamma$  channel, while  $(1/\sqrt{6})$  is the appropriate Schmid factor for the active {111}<110> slip system. As stated above at 850°C  $\sigma_{3a} = 50$  MPa while  $\sigma_{1t} = -433$  MPa. The available evidence [25] indicates that the misfit stresses are largest at the highest temperatures and extrapolate to small values at room temperature. Misfit stresses at any other temperature can be obtained by linear interpolation. Three incubation times measured under different stresses and temperatures serve to evaluate the three unknowns  $Q$ ,  $V^*$  and  $v_0$  in equation (2). These incubation times,  $t_i$ , and their conditions are given in Table 2. Considering the incubation process to result from percolation of dislocation loops between regions of ingrown dislocations at an average spacing of  $\Lambda$  in the volume we have

$$\frac{\Lambda}{t_i} = \beta v_0 \exp \left( -\frac{Q - (\tau - \tau_{or})V^*}{kT} \right) \quad (4)$$

where  $\beta$  is an attenuation factor accounting for the need of dislocation motion along the low stressed vertical  $\gamma$  channels in bridging the gap between the grown-in dislocation sources. The distance  $\Lambda$  was estimated from Fig. 1 and several low magnification TEM micrographs to be about 50  $\mu\text{m}$ . From the incubation data given in Table 2 we readily determine that

$$Q = 1.094 \times 10^{-11} \text{ ergs} = 658 \text{ kJ/mol} \quad (5a)$$

$$V^* = 7.44 \times 10^{-22} \text{ cm}^3. \quad (5b)$$

Furthermore, we determine  $v_0$  from a more direct observation of the type given in Figs 8–10 where dislocations are known to spread out only along the horizontal  $\gamma$  channels that are uniformly highly stressed†. From these figures it is established that at 825°C under an applied stress of 450 MPa the percolating dislocation front moves a total distance of 5  $\mu\text{m}$  during a period of 120 s. This gives directly

$$v_0 = 1.63 \times 10^{21} \text{ cm/s} \quad (5c)$$

which is exceedingly high. Moreover, using this value of  $v_0$  with  $A = 50 \mu\text{m}$  it is possible to determine the attenuation factor  $\beta$  from any of the three incubation measurements given in Table 2, as

$$\beta = 5.24 \times 10^{-2}. \quad (5d)$$

Finally, with this information we estimate the incubation time at 900°C under a stress of 552 MPa and find it to be 21 s. This is indeed very short and on the verge of being difficult to detect. Experimentally, there was no incubation period detected at 900°C.

The solid solution-drag-controlled-velocity given in equation (2) can be re-stated in another form with the stress dependence of the activation free energy given by [26]

$$\Delta G^* = \Delta F_0[1 - (\tau/\dot{\tau})] \quad (6)$$

where

$$\Delta F_0 = Q \quad \text{and} \quad \dot{\tau} = Q/V^* \quad (7a, b)$$

are the Helmholtz free energy barrier of the controlling obstacle at vanishing stress and the back extrapolated athermal flow stress at 0 K that is 1.47 GPa. Moreover, by related considerations it is possible also to define a characteristic temperature  $T_0$  where the resistance would vanish

$$T_0 = \Delta F_0/k \ln(\dot{\gamma}_0/\dot{\gamma}) \quad (8)$$

where  $\dot{\gamma}_0 = b\rho_m v_0$  can be taken as an associated pre-exponential factor of such a solid solution controlled strain rate. Taking a mobile dislocation density  $\rho_m = 10^{10} \text{ cm}/\text{cm}^3$  as reasonable (where all dislocations in steady state deformation are considered mobile),  $\dot{\gamma}_0$  can be estimated to be  $4 \times 10^{23}/\text{s}$ . This gives for  $T_0 = 1140 \text{ K}$  (for a shear strain rate of  $2 \times 10^{-7}/\text{s}$ ). While the above values of the solid solution resistance are fully consistent with the measured parameters of the incubation phenomenon, it is clear that they are not all reasonable. The activation energy  $Q$  (or  $\Delta F_0$ ) is quite high resulting in a substantial  $T_0$  and also a very high pre-exponential factor for the velocity. Only the activation volume at a level of  $47.5b^3$  is of a reasonable magnitude. It is possible that the temperature dependence of the misfit stresses are somewhat different from what has been considered in Appendix I. The experimentally measured incubation parameters may have also been influenced by variations in the networks of grown-in dislocations in individual test samples. These factors could markedly affect the calculated value of  $Q$ . Nevertheless, the parameters established above are quite useful for operational purposes.

While the above form given in equation (2) of the solid solution resistance is mechanically preferable, it is also possible to state it in a power law form as, e.g.

$$v = v_0 \left( \frac{(\tau - \tau_0)V^*}{kT} \right)^m \exp\left(-\frac{Q}{kT}\right). \quad (9)$$

If this is done the effective power law exponent  $m$  is found to be 11.97.

Finally, the solid solution drag on the dislocations can be represented as a solid solution resistance  $\tau_{ss}$  which can be written in the following form

$$\tau_{ss} = \hat{\tau}_{ss}[1 - (kT/Q)\ln(\dot{\gamma}_0/\dot{\gamma})] \quad (10)$$

where  $\hat{\tau}_{ss} = 1.47 \text{ GPa}$  as determined in equation (7b),  $Q = 658 \text{ kJ/mol}$ , and  $\dot{\gamma}_0 = 4 \times 10^{23}/\text{s}$ . We note that the shear strain rate  $\dot{\gamma}$  in equation (10) is the actual glide rate in  $\gamma$  channels, which should relate to the tensile strain rate  $\dot{\epsilon}$  on the  $\langle 001 \rangle$  crystal simply by a relation of

$$\dot{\epsilon} = (1 - c)\beta\dot{\gamma} \quad (11)$$

where  $\beta (= 1/\sqrt{6})$  is the appropriate Schmid factor for the effective slip system and  $c (= 0.7)$  is the volume fraction of the  $\gamma'$  phase. For a typical case of 850°C at a total steady state strain rate of  $2.5 \times 10^{-8}/\text{s}$  the resolved solid solution shear resistance in the  $\gamma$  channels should be 17.5 MPa.

In summary, it is clear that the incubation period arises from the "slow" filling of the matrix by creep dislocations. Dislocations that emanate from grown-in clusters must penetrate through the cross section of the sample, against the combined resistance of Orowan bowing and the solid solution drag under the applied stresses assisted by the misfit stresses. Thus, the length of the incubation period will sensitively depend on the applied stress and temperature, as well as on the  $\gamma/\gamma'$  microstructure and the distribution of the networks of grown-in dislocation clusters acting as sources.

### 5.5. Dislocation resistance

At steady state the dislocations in the  $\gamma$  channels are expected to offer some resistance to each other in terms of a dislocation resistance  $\tau_{dis}$ . This can be estimated from a relation

$$\tau_{dis} \approx \alpha \mu b \sqrt{\rho} \quad (12a)$$

or

$$\tau_{dis} = [1/8\pi(1-\nu)](\mu b/h) \quad (12b)$$

based on well known forms for interactions at random encounters [ $\alpha \approx 0.1$ , in equation (12a)] or for the passage resistance of two opposite edge dislocations a distance of  $h$  apart [equation (12b)]. Both would result in an estimate of about 10–12 MPa. We note that this resistance is small and is to a large extent already represented by the Orowan resistance where the extrusion of dislocations into the narrow  $\gamma$  channels is considered. The dislocation resistance should, however, be effective for the entry of other dislocations into  $\gamma$  channels that are already occupied by a primary set of dislocations. We consider this as a possibility at steady state, where knitted space networks of dislocations are found in  $\gamma$  channels, indicating the interpenetration of at least two sets

of dislocations emanating from two separate pre-existing linear tangles.

### 5.6. Deformation during primary and steady state creep

During the primary transient, dislocations continue to fill the matrix material by bowing between the  $\gamma'$  precipitates on  $\{111\}$  planes. The common feature of the microstructure during the early stages of primary creep is the presence of  $a/2\langle 110 \rangle$  dislocations at the  $\gamma/\gamma'$  interfaces lying at angles of  $45^\circ$  to the precipitate faces. These are mixed dislocations, with Burgers vectors at  $60^\circ$  to the line direction. During the early stages of the transient, the  $\gamma$  phase channels are locally filled with dislocations of a single  $a/2\langle 110 \rangle$  Burgers vector, but as the end of the transient is approached, dislocations with other Burgers vectors emanating from other sources interpenetrate, leading to reactions, forming the observed networks and in the process preventing significant crystallographic rotations that would have resulted from single slip. The majority of the dislocations have Burgers vectors of the stressed slip systems, but reactions between these primary dislocations also produce some  $a/2[110]$  and  $a/2[\bar{1}10]$  dislocations which are often edge in orientation. The operation of multiple slip systems and uniform filling of the matrix material by the Orowan bowing of the dislocations, efficiently establishes a three-dimensional network of dislocations in the  $\gamma$  channels. As stated in Section 5.5 above, the resulting strain hardening is relatively modest.

The "steady state" three-dimensional network of dislocations is somewhat irregular, with spacings and arrangements varying from channel to channel. This is due to the fact that it was formed from creep dislocations as they penetrated into individual channels. A large fraction of the dislocations which form the network are associated with the  $\gamma/\gamma'$  interfaces. These are now not very planar and as clearly defined as they were in primary creep. Assuming that the dislocations associated with the interfaces during steady state creep are still  $60^\circ$  dislocations, and resolving their edge components into the interfaces, a dislocation spacing of 42 nm would be required to relieve a misfit of  $-0.305\%$  if only these  $60^\circ$  dislocations were present. However, during steady state creep the  $60^\circ$  dislocations as well as some  $a/2[110]$  and  $a/2[\bar{1}10]$  edge dislocations with Burgers vectors contained in the plane of the interface were also present. The average spacing observed during steady state creep was in the range 60 to 80 nm, so it appears that the misfit between the  $\gamma$  and  $\gamma'$  phases is largely relieved. (We note that a series of pure edge dislocations with a spacing of 84 nm are required for complete misfit relief.) The observed dislocation spacings increase to 80–100 nm and are more regularly distributed after 750 h of annealing at 850°C. However, the networks that actually develop during steady state creep are often quite irregular. Neverthe-

less, the available evidence suggests that the misfit stresses must be nearly eliminated during primary creep. As discussed in Section 5.4, during the incubation period in a tension experiment the horizontal  $\gamma$  channels are favored for dislocation motion because of favorable misfit stresses while the vertical  $\gamma$  channels show little activity. Once the initial dislocation percolation is achieved through the structure, this favored deformation of the horizontal  $\gamma$  channels should continue during primary creep until the misfit stresses are neutralized. In fact we conclude that primary creep in virgin crystals is entirely a result of the elimination of misfit stresses. This is readily verifiable. The creep curves in Fig. 3 indicate that the total primary creep strain is about  $5 \times 10^{-4}$  which translates into a glide strain increment of  $\Delta\gamma = 4.1 \times 10^{-3}$  in the  $\gamma$  channels. If this inelastic strain increment were to neutralize a built-in resolved shear stress due to elastic misfit the latter could be of a magnitude of  $\Delta\sigma = \mu\Delta\gamma = 198$  MPa. This is almost exactly what results from the FEM analysis presented in Section 6. Once the primary creep is accomplished and the misfit stresses are eliminated by it, subsequent stress changes produce no important additional transients.

### 5.7. Impenetrability of the $\gamma'$ phase precipitates

While the creep resistance of the assembly of the heterogeneous  $\gamma/\gamma'$  microstructure is accountable by the deformation resistance of the  $\gamma$  phase alone, and the negative pressures that build up in it, that we will discuss in Section 6 below, the key to this behavior is the non-deformability of the  $\gamma'$  precipitates. The TEM observations reported above have amply demonstrated that until the very late stages of the creep deformation when dislocations can finally be observed to enter the  $\gamma'$  particles, the latter remain undeformable, and free of dislocations. Since  $\gamma'$  phases of comparable composition are quite deformable in bulk [28, 29], it must be concluded that the absence of deformation in the  $\gamma'$  phase is more a problem of penetration of the  $\gamma$  dislocations into the  $\gamma'$  particles rather than a high glide resistance of the particles themselves. Thus, shearing of the heterogeneous microstructure on any coherent octahedral plane must require repeated nucleation of entry configurations of dislocations in the  $\gamma'$  particles from the  $\gamma/\gamma'$  interfaces.

Well developed theories exist for the process of  $\gamma'$  shearing in nickel base alloys with low to intermediate volume fractions of spherical  $\gamma'$  precipitates, and these have been recently reviewed by Nembauch and Neite [30]. In these theories, long free segments of dislocations contact and partially loop the spherical precipitates, reducing the stress required for creation of an APB. For high volume fraction single crystal alloys with cuboidal precipitates, it is necessary to account for the very localized nature of deformation by dislocation bowing out into individual matrix channels without the possibility of looping the pre-

cipitates and as well as the buildup of complex stresses in the creep flow problem. Here we will consider the most likely sequences of configurations involved in the penetration of  $\gamma'$  dislocations into  $\gamma'$  particles.

In the later stages of creep at 850°C in CMSX-3, the dominant mode of  $\gamma'$  shearing is by APB coupled pairs of  $a/2\langle 110 \rangle$  dislocations. Caron and Khan have also observed this mode of shearing at 760°C and 1050°C in CMSX-3 [3]. Further dissociation of the superpartials into Shockley partials is possible, and creates a complex stacking fault within the  $\gamma'$  [8]. With weak beam microscopy the APB-coupled  $a/2\langle 110 \rangle$  dislocations are normally resolved in Ni<sub>3</sub>Al [31–35]. For this calculation an APB energy of 0.11 J/m<sup>2</sup> [35] will be considered as representative. Further dissociation of the  $a/2\langle 110 \rangle$  dislocations into Shockley partials in the  $\gamma'$  is only rarely observed [32] and the measurement of the complex stacking fault energy is difficult since the dissociations are at the limit of the weak beam technique. For CMSX-2, Caron and Khan [36] report unresolvable (<2 nm) complex stacking faults, and for this reason the fault energy will be taken to be 0.09 J/m<sup>2</sup>. Although the matrix stacking fault energies are likely to be slightly lower, we will assume that the degree of dissociation is similar.

In the problem of interest to us here we distinguish two types of full dislocations: the mixed (60°)  $\gamma$  phase dislocations pressed against the  $\gamma/\gamma'$  interface in the horizontal channels (Burgers vector making an angle of 60° with the dislocation line), identified hereafter with a subscript (m); and the screw dislocations in the vertical channels pressed against the  $\gamma'$  particles in like fashion, identified hereafter with a subscript (s). The line energies of these two internally dissociated extended dislocations are

$$\epsilon_m = \frac{\mu b^2}{4\pi(1-\nu)} \left( \frac{4-\nu}{4} \right) \ln \left( \frac{\alpha R}{b} \right) - \frac{\mu b^2}{12\pi(1-\nu)} \ln \left( \frac{\alpha \delta_m}{eb} \right) \quad (13a)$$

$$\delta_m = \frac{\mu b^2}{12\pi(1-\nu)\chi_{SF}} \quad (13b)$$

$$\epsilon_s = \frac{\mu b^2}{4\pi} \ln \left( \frac{\alpha R}{b} \right) - \frac{\mu b^2}{24\pi} \left( \frac{2-3\nu}{1-\nu} \right) \ln \left( \frac{\alpha \delta_s}{eb} \right) \quad (14a)$$

$$\delta_s = \frac{\mu b^2}{24\pi\chi_{SF}} \left( \frac{2-3\nu}{1-\nu} \right) \quad (14b)$$

where  $\delta_m$  and  $\delta_s$  are the equilibrium separations of the Shockley partials in the mixed dislocations and screw dislocation respectively, considering the alloy as elastically isotropic with shear modulus  $\mu$  and Poisson's ratio  $\nu$ . In these equations  $b$  is the magnitude of the Burgers vector of the full dislocation,  $R$  is the usual outer cut-off distance for the dislocation strain field, and  $\alpha$  is the usual core cut-off parameter

[37] and  $e = 2.718$ . The appropriate magnitudes of these will be taken up later.

Thermally assisted penetration of dislocations into the  $\gamma'$  phase should occur in the form of a superdislocation in a configuration sketched out in Fig. 23(a) and (b). An analysis of this process, given in greater detail in Appendix II gives the activation energy expressions  $\Delta G_m^*$  and  $\Delta G_s^*$  for entry of superdislocations into the  $\gamma'$  particles from horizontal channels in the form of 60° mixed dislocations and from vertical channels in the form of screw dislocations respectively as

$$\Delta G_m^* = A_m(\mu b^3) \frac{\left\{ \ln \left[ e \left( \frac{\chi_{APB}}{\mu b} \right) \left( \frac{\mu}{\tau} \right) \right] \right\}^{3/2}}{(\tau/\mu)} \quad (15a)$$

$$A_m = \frac{1}{3} \left( \frac{4-\nu}{4\pi(1-\nu)} \right)^2 \left[ \ln \left( \frac{\alpha R}{b} \right) - \frac{1}{2} \ln \left( \frac{\alpha \Delta_m}{eb} \right) - \frac{1}{3(4-\nu)} \ln \left( \frac{\alpha \delta_m}{eb} \right) \right]^{1/2} \quad (15b)$$

$$\Delta_m = \frac{\mu b^2}{2\pi(1-\nu)\chi_{APB}} \left( \frac{4-\nu}{4} \right) \quad (15c)$$

and

$$\Delta G_s^* = A_s(\mu b^3) \frac{\left\{ \ln \left[ e \left( \frac{\chi_{APB}}{\mu b} \right) \left( \frac{\mu}{\tau} \right) \right] \right\}^{3/2}}{(\tau/\mu)} \quad (16a)$$

$$A_s = \frac{1}{3\pi^2} \left[ \ln \left( \frac{\alpha R}{b} \right) - \frac{1}{2} \ln \left( \frac{\alpha \Delta_s}{eb} \right) - \frac{(2-3\nu)}{12(1-\nu)} \ln \left( \frac{\alpha \delta_s}{eb} \right) \right]^{1/2} \quad (16b)$$

$$\Delta_s = \frac{\mu b^2}{2\pi\chi_{APB}} \quad (16c)$$

where  $\Delta_m$  and  $\Delta_s$  are the equilibrium widths of the APB zones of the 60° mixed superdislocation and the screw superdislocation respectively.

In addition to the activation free energies of the saddle point configurations of the nucleated superdislocation bulges in the  $\gamma'$  particle, the actual sizes and shapes of the entry configurations are also of interest. These can be obtained separately (see Appendix II) and are

$$\frac{A_m^*}{b} = \frac{12\pi(1-\nu)A_m}{(4-\nu)} \frac{\left\{ \ln \left[ e \left( \frac{\chi_{APB}}{\mu b} \right) \left( \frac{\mu}{\tau} \right) \right] \right\}^{1/2}}{(\tau/\mu)} \quad (17a)$$

$$\frac{\lambda_m^*}{b} = \frac{(4-\nu)}{16\pi(1-\nu)} \frac{\ln \left[ e \left( \frac{\chi_{APB}}{\mu b} \right) \left( \frac{\mu}{\tau} \right) \right]}{(\tau/\mu)} \quad (17b)$$

$$\frac{A_s^*}{b} = 3\pi A_s \frac{\left\{ \ln \left[ e \left( \frac{\chi_{APB}}{\mu b} \right) \left( \frac{\mu}{\tau} \right) \right] \right\}^{1/2}}{(\tau/\mu)} \quad (18a)$$

$$\frac{\lambda_s^*}{b} = \frac{1}{4\pi} \frac{\ln \left[ e \left( \frac{\chi_{APB}}{\mu b} \right) \left( \frac{\mu}{\tau} \right) \right]}{(\tau/\mu)} \quad (18b)$$

where  $\lambda_m^*$  and  $\lambda_s^*$  are the amplitudes of the saddle point bulges for the mixed  $60^\circ$  superdislocation and screw superdislocation respectively.

The stress dependences of  $\Delta G^*$ ,  $A^*$  and  $\lambda^*$  are of interest and have been calculated for the following quantities that are considered appropriate for the  $\gamma$  and  $\gamma'$  crystal structures at  $850^\circ C$

$$\mu = 48.2 \text{ GPa} \quad [25]$$

$$v = 0.276 \quad [37]$$

$$b = 0.254 \text{ nm}$$

$$\chi_{SF} = 0.09 \text{ J/m}^2$$

$$\chi_{APB} = 0.111 \text{ J/m}^2 \quad [35].$$

With these values the following relevant dissociation dimensions of the dislocations are found

$$\delta_m/b = 3.59 \quad (19a)$$

$$\delta_s/b = 2.10 \quad (19b)$$

$$\Delta_m/b = 20.1 \quad (19c)$$

$$\Delta_s/b = 15.6. \quad (19d)$$

These magnitudes are consistent with available weak beam measurements mentioned above, and also discussed below. With these dissociation dimensions the scale factor coefficients for the mixed dislocation  $A_m$ , and the screw dislocation  $A_s$ , are found to be:  $A_m = 0.128$ ,  $A_s = 0.078$ . Utilizing these dissociation dimensions and the scale factor coefficients, the stress dependence of  $\Delta G_m^*$ ,  $\Delta G_s^*$ ,  $A_m^*/b$ ,  $A_s^*/b$  and  $\lambda_m^*/A_m^* \approx \lambda_s^*/A_s^*$  has been calculated and is plotted in Fig. 24, where the following abbreviation was introduced

$$B_m = 12\pi(1-v)A_m/(4-v) \quad (19e)$$

$$B_s = 3\pi A_s. \quad (19f)$$

We now note that  $A_m(\mu b^3) = 0.632 \text{ eV}$  and  $A_s(\mu b^3) = 0.385 \text{ eV}$  respectively. Thus, considering that at a temperature of  $850^\circ C$  it is unreasonable to expect a thermal fluctuation much larger than  $3.75 \text{ eV}$  on the average, (corresponding to  $1.0 \text{ eV}$  at room temperature) we must reach two important conclusions. First, that the preferred penetration of  $\gamma'$  particles will be by screw dislocations from the vertical channels, and second, that this is not likely to be at a resolved shear stress ratio  $\tau/\mu$  much less than 0.02, or an actual resolved shear stress less than  $965 \text{ MPa}$ , which translates into a tensile stress of  $2.36 \text{ GPa}$ . These are stresses far in excess of those for which penetration of  $\gamma'$  particles is observed. To insert the pair of  $\gamma$  dislocations into the  $\gamma'$  particles as a superdislocation, as depicted in Fig. 23(a) and (b), it is necessary that the  $\gamma'$  phase resists the entry of the leading  $\gamma$  screw

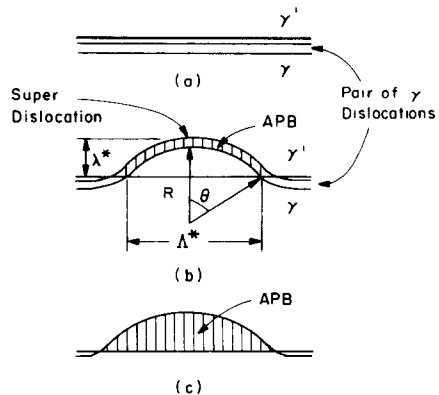


Fig. 23. Forms of penetration of dislocations from the  $\gamma$  phase into the  $\gamma'$  particles: (a) a pair of extended  $\gamma$  dislocations are pressed against the  $\gamma'$  particles prior to penetration; (b) the pair of  $\gamma$  dislocations has entered into the  $\gamma'$  particle as a nucleus of a superdislocation; (c) an individual  $\gamma$  dislocation penetrating the  $\gamma'$  particle at the expense of leaving behind an anti-phase boundary.

dislocation of the pair until the energy difference between the pair of screws and the screw superdislocation is reduced to the levels calculated by us above. This will occur only for APB energies in excess of  $0.49 \text{ J/m}^2$ . However, the leading screw dislocation can enter the  $\gamma'$  particle all along the interface at a much lower stress level by leaving an APB behind it, as shown in Fig. 23(c). The threshold resolved shear stress  $\tau_1$  that is required for this (as the bowout radius  $R \rightarrow \infty$ ) is simply

$$\tau_1 = \chi_{APB}/b \quad (20)$$

which, for the magnitude of the APB energy given above, is only  $437 \text{ MPa}$ . Further calculations show that slightly higher stresses are required at finite values of  $R$  [25], and again penetration by screw dislocations in the vertical matrix channels is favored.

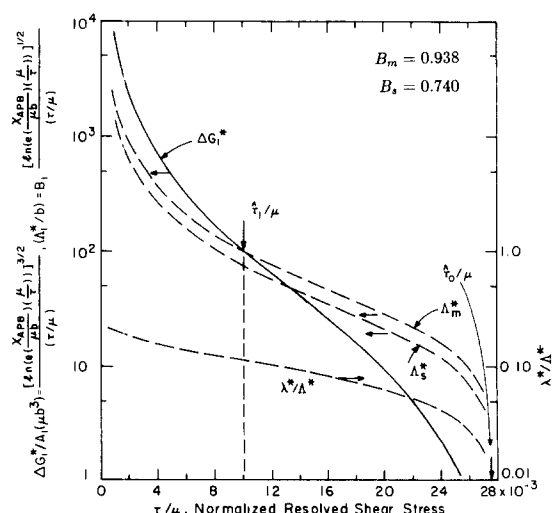


Fig. 24. The stress dependence of the activation free energy, for the penetration of the  $\gamma$  dislocations into the  $\gamma'$  particles, and the stress dependence of the geometry of the saddle point configuration.

Furthermore, if a pair of dislocations on the same plane had been pressing against the  $\gamma'$  particle as discussed above, for the superdislocation insertion mode of penetration, then, the pressure of the second dislocation as a pile up, lends a stress concentration of 2 that reduces the required resolved shear stress down to 219 MPa. Thus, we conclude that for the fault energies characteristic of CMSX-3, penetration of the  $\gamma'$  particles should be by individual  $\gamma$  dislocations of either mixed or screw type, leaving behind APBs, occurring at a resolved shear stress between 219 and 437 MPa. Once a single dislocation has entered the  $\gamma'$  particle and has left an APB behind, the entry of a second dislocation on the same plane should be strongly favored to eliminate the APB, as is usually observed experimentally. The lower of the resolved shear stresses is generated locally only during the later stages of creep at 219 MPa. Insertion of pairs of dislocations as depicted in Figs 23(a) and (b) should then only occur for APB energies above  $0.49 \text{ J/m}^2$ , where the leading screw dislocation can be held up at the interface for the required penetration configuration to be attained. From this it follows that within a given alloy system, microstructures which contain high volume fractions of cuboidal precipitates should have a higher resistance of  $\gamma'$  shearing, relative to a microstructure containing a low volume fraction of spherical  $\gamma'$  precipitates, since the possibility of looping the isolated spherical precipitates gives a net line energy reduction for penetration of dislocations in the  $\gamma'$ . However, the resistance to shearing in high volume fraction  $\gamma'$  alloys containing cuboidal precipitates is still largely dependent, as is the resistance for alloys containing spherical precipitates [38], on the APB energy, and the buildup of local stresses sufficient to push dislocations into the precipitates.

It should also be noted that dislocations looped around the corner of precipitates on a  $\{111\}$  plane, by similar analysis, would penetrate into the  $\gamma'$  particle at a stress level slightly lower than 219 MPa, but long, free segments of dislocations encircling the  $\gamma'$  particles, without being incorporated into the three dimensional network were, however, rarely observed in the TEM micrographs during steady state creep.

### 5.8. Recovery

In order to construct a physically meaningful constitutive model for the creep process it is necessary to understand the details of the mechanisms by which dislocations move through the material as well as the mechanisms which govern the recovery processes. In the case of the nickel base single crystals of  $\gamma$  and  $\gamma'$  phases under the conditions studied here, there must be some critical rearrangements of the dislocations contained in the matrix  $\gamma$  phase for maintenance of a steady state during creep.

Direct and indirect methods of studying the recovery processes have been pursued. Following the establishment of steady state creep, a sample was

unloaded and held at the creep temperature to permit time for static (diffusion controlled) recovery processes to proceed. Reloading transients after extended rest periods of the order of  $1-2 \times 10^4$  s were so slight that they were difficult to even measure, indicating that diffusional processes under no stress were ineffective in causing dislocation rearrangements in the matrix over these time periods. This demonstrates that the retained dislocation networks have the aspect of being geometrically necessary to neutralize the misfit stresses between  $\gamma$  and  $\gamma'$  phases. *In situ* annealing experiments also showed few important rearrangements of the matrix dislocations at temperatures of  $850^\circ\text{C}$  or lower over periods of observation of  $1-4 \times 10^4$  s. Measurable recovery effects were, however, found at  $850^\circ\text{C}$  for recovery times of the order of  $1-4 \times 10^6$  s. The *in situ* observations also indicated that static recovery becomes important at temperatures above about  $900^\circ\text{C}$ , which interestingly is also the temperature range where the precipitates begin to raft at noticeable rates. Considering the stability of the three-dimensional networks which buildup during creep at low to intermediate temperatures, and also the lack of "extra" dislocations in the structure, it is probably not altogether surprising that static recovery is ineffective in promoting further creep deformation. Furthermore, the high creep stress exponents and activation energies for creep observed in nickel base superalloys offer no direct support for creep which is diffusion controlled. For these reasons, models which assume that the rate limiting mechanism for creep is diffusion controlled static recovery or climb of free segments of dislocations around  $\gamma'$  precipitates can not adequately describe the creep deformation process at temperatures less than about  $900^\circ\text{C}$  in these nickel base single crystals of high  $\gamma'$  volume fraction. Instead it appears that a more detailed model which includes a stress assisted dynamic recovery mechanism where dislocations mutually cancel in local areas of the channels is necessary to formulate a realistic model for the apparent stationary state in the dislocation structure. How this is to be accomplished remains unclear.

While evidence for the absence of diffusion controlled recovery is strong it is interesting to note that evidence of diffusional processes were observed during deformation—based on two separate observations.

First, we recall that the temperature and stress dependence of the minimum creep rate gives an apparent activation energy of 495 kJ/mol and a stress exponent of 7.1. In comparison, the activation energy of the solid solution drag controlled velocity of dislocations was found to be 659 kJ/mol with an apparent stress exponent of  $m = 11.97$  for a power law representation of the solid solution velocity. These activation parameters determined from the incubation response are quite a bit larger than those from the steady state response suggesting that they

are governed by considerations of thermally activated glide as was assumed. In comparison, the much lower activation parameters for steady state creep suggest that they must be influenced to some extent by some diffusional process.

Second, there is direct evidence in the dislocation structures of diffusional smoothing processes. In Figs 8–10 there are many examples of cross glide processes of the lead screw dislocation that lays down trailing dipoles of  $60^\circ$  mixed dislocations behind it. When such a cross glide event occurs it should result in a sharp  $90^\circ$  angle in the dipole left behind. As the micrographs show, in, e.g. at point B of Fig. 10, the sharp corner is rapidly rounded out during the time increment when the screw dislocation has gone from B to C. Since the dipoles are of  $60^\circ$  mixed nature such rounding out requires a combination of core diffusion and volume-diffusion-controlled-climb of these dislocations that are left behind. This climb continues monotonically during the creep process to straighten out the layed down dipoles and gradually turns them into directions parallel to the cube directions. This can be discerned in Fig. 11(a) and (b) where the more recently layed down dislocations are parallel to the  $\langle 110 \rangle$  directions while the older ones seem to gradually rotate around to become nearly parallel to the  $\langle 100 \rangle$  directions where they substantially reduce their line length. In Section 6.5 we obtain an estimate of the effective diffusion constant determined from the rate of rounding of initially sharp corners in the  $60^\circ$  dislocations of the type shown in Fig. 10. This gives an effective diffusion constant of  $3.1 \times 10^{-16} \text{ cm}^2/\text{s}$  at  $850^\circ\text{C}$ . With a diffusion constant of this low magnitude the effective diffusional transport times over  $\gamma'$  particle dimensions can be estimated to be of the order of  $10^6 \text{ s}$ . This is in agreement with the observed recovery times at  $850^\circ\text{C}$  discussed in Section 6.5.

## 6. ANALYSIS OF MACROSCOPIC DEFORMATION RESISTANCES

### 6.1. Approximate analytical model of the $\gamma - \gamma'$ composite

As mentioned in the introduction, and as discussed by us earlier in outline [13–15], the restriction of creep deformation into the narrow  $\gamma$  phase channels sets up substantial gradients of pressure and negative pressure in the channels. These arise because of the effective frictional drag that the non-deforming  $\gamma'$  particles impose on the  $\gamma$  “fluid”, in its flow from the vertical channels into the horizontal channels. The integrated negative pressures over the horizontal  $\gamma$  channels offer considerable load support and substantially elevate the tensile creep resistance of the heterogeneous single crystals strained in the  $\langle 001 \rangle$  direction.

In the CMSX-3 single crystals the thin layers of creeping  $\gamma$  phase matrix are surrounded by rigid, non-deforming precipitates. This is comparable to the

well known three dimensional plasticity problem of compression of thin disks between rigid platens, first described by Schroeder and Webster [39]. In their analysis, a pressure gradient, or “friction hill”, builds up in the deforming thin disk due to frictional sticking between the disk and platens. The pressure gradient increases the average load carrying ability of the material, and as the aspect ratio of the disk becomes larger, increasingly higher applied loads are required to deform the material. When there is no slippage along the interface, the average applied compressive stress,  $P$ , required to deform a disk of material with an equivalent bulk tensile plastic resistance  $\sigma_0$  gives an average factor of increased load carrying ability  $(P/\sigma_0)_{\text{avg}}$  of

$$\left(\frac{P}{\sigma_0}\right)_{\text{avg}} = 1 + \frac{2k}{3} \left(\frac{R}{t}\right) \quad (21)$$

where  $R$  is the disk radius,  $t$  is the thickness, and  $k$  is a constant equal to 0.577, in the case where no slippage occurs between disk and platens.

Considering the reverse problem of pulling on a thin disk in tension, a *negative* pressure gradient develops in the radial direction of the disk, monotonically rising from the outer edge of the disk at  $r = R$  toward its center at  $r = 0$ . The resulting normal stress distribution is

$$\frac{\sigma(r)}{\sigma_0} = 1 + 2k \left(\frac{R}{t} - \frac{r}{t}\right) \quad (22)$$

where  $\sigma(r)$  is now the tensile stress at a distance  $r$  from the center of the disk and  $\sigma_0$  is the equivalent tensile plastic resistance of the disk material.

To use the Schroeder and Webster analysis to estimate the net effect of the frictional constraint of the  $\gamma'$  precipitate in the two phase material, it is necessary to consider not only the problem of thickening matrix channels normal to the applied stress but also compressing channels parallel to the applied stress. By superposition of two disks at right angles as shown in Fig. 25, the total average increase in load carrying ability is approximately

$$\left(\frac{P}{\sigma_0}\right)_{\text{avg}}^{\text{tot}} = 2 \left[ 1 + \frac{2k}{3} \left( \frac{R}{t} \right) \right]. \quad (23)$$

The total average increase in load carrying ability of the  $\gamma/\gamma'$  microstructure over that of the matrix material, deforming freely, can then be estimated using the characteristic microstructural dimensions of

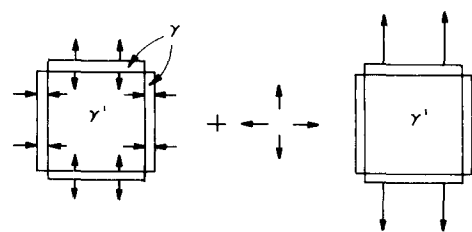


Fig. 25. Sketch showing the deforming  $\gamma$  phase as slabs being plastically compressed or extended between rigid  $\gamma'$  platens.

the  $\gamma/\gamma'$  material which suggest the replacement  $R/t = L/(h\sqrt{\pi})$ , where  $L$  is the channel length and  $h$  the matrix channel thickness. For a channel length of  $0.45 \mu\text{m}$  and thickness of  $60 \text{ nm}$ ,  $L/(h\sqrt{\pi}) = 4.23$ , which gives a calculated factor of increase in average load carrying ability of the  $\gamma/\gamma'$  material to be  $(P/\sigma_0)_{\text{avg}}^{\text{tot}} = 5.34$ , in the limit of no slippage.

The tensile creep resistance of a Ni-6W solid solution alloy at  $854^\circ\text{C}$  and at a reference strain rate of  $2.5 \times 10^{-8}/\text{s}$  is 35 MPa [27]. Taking the above value of 35 MPa for  $\sigma_0$ , a pair of thin slabs of nickel solid solution with dimensions characteristic of the matrix channels in the  $\gamma/\gamma'$  material should then have an average tensile creep resistance of  $P = (35 \text{ MPa})(5.34) = 187 \text{ MPa}$ . This falls quite short of the experimentally observed tensile creep resistance of CMSX-3 single crystals in the  $\langle 001 \rangle$  orientation of 552 MPa. As already discussed in Section 5 above, and as reported by us earlier [13-15], the effective deformation resistance of the  $\gamma$  channels in the CMSX-3 crystals is far in excess of the 35 MPa bulk tensile resistance of the Ni-6W solid solution alloy quoted above or the solid solution resistance of 43 MPa calculated for the matrix material in Section 5.4 because of their substantial Orowan resistance. Before attempting to use the actual deformation resistance of the  $\gamma$  matrix in equation (23) or any necessary variant of it, we report below the results of a more accurate finite element study of the flow of a creeping "fluid" in the narrow channels of a  $\gamma/\gamma'$  microstructure.

### 6.2. Finite element analysis of the thermal misfit stresses in the $\gamma/\gamma'$ microstructure

The finite element model (FEM) for computing the initial thermal misfit stresses and the creep flow problem in the CMSX-3 microstructure was formulated using generalized plane strain elements. These elements allow uniform displacement in the "thickness" direction of the mesh by allowing displacement of a single node which is fixed to a plane in the third dimension of the model. This permits uniform deformation in the third dimension as well as the development of the associated stresses in this direction. The generalized plane strain analysis offers a very good approximation of the three-dimensional problem for small strains.

Utilizing the symmetry of the microstructure, it is only necessary to model one quarter of the  $\gamma'$  precipitate with its adjacent matrix. The mesh is shown in Fig. 26, where the shaded portion corresponds to the matrix material, and the unshaded area to the precipitate. The matrix channel parallel to the upper boundary in Fig. 26 (parallel to the 1 direction) will be referred to as the horizontal channel, while the channel parallel to the right border will be referred to as the vertical channel. Loads or prescribed displacements were applied along the 2 direction, normal to the horizontal channel. This direction corresponds to the  $\langle 001 \rangle$  direction in the single

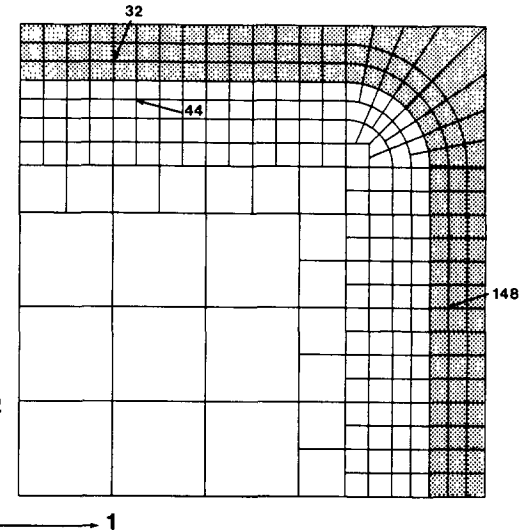


Fig. 26. The finite element mesh of the  $\gamma/\gamma'$  problem. The shaded area corresponds to the deforming  $\gamma$  matrix material.

crystal, which is the usual orientation of the loading axis in most applications of commercial single crystal components. As can be seen, the model was formulated in a way which would preserve the channel dimensions relative to the microstructure, but since a generalized plane strain analysis is done, the volume fraction of the  $\gamma'$  is somewhat higher here than in the actual material because the matrix channels parallel to the plane of the mesh have been neglected. It should also be noted that the  $\gamma/\gamma'$  boundary is tied together by common nodes along the boundary, which do not permit sliding. The "coherency" of the precipitate is then effectively enforced by the model. The consequences of this requirement will be discussed later.

Since thermal misfit between the  $\gamma$  and  $\gamma'$  phases in CMSX-3 crystals is substantial and has important ramifications in the initiation of creep deformation, these stresses were introduced into the model by differential thermal expansion of the  $\gamma$  and  $\gamma'$  phases. The coefficients of thermal expansion for the individual phases of the CMSX-3 crystal were estimated using published data [23, 24]. Assuming again that the misfit at room temperature is zero [25], and using the estimated coefficients of expansion  $\alpha_\gamma = 1.63 \times 10^{-5}/^\circ\text{C}$  and  $\alpha_{\gamma'} = 1.26 \times 10^{-5}/^\circ\text{C}$  gave an unconstrained thermal misfit of  $-0.305\%$  at  $850^\circ\text{C}$ . This value is slightly lower than the value reported by Fredholm and Strudel [17] for their measurement of dislocation spacings after aging in CMSX-2 at  $1050^\circ\text{C}$ , and is slightly higher than the high temperature X-ray measurement of Nathal *et al.* [22] for a somewhat similar alloy.

The elastic constants of the matrix and the precipitate of CMSX-3 were estimated from the best available data for materials with similar compositions. For the matrix material the data for pure Ni from  $25-487^\circ\text{C}$  listed by Simmons and Wang [40] was extrapolated to  $850^\circ\text{C}$ . The elastic compliances

obtained as such were nearly identical to those of DS Mar-M-247 at 850°C [41], i.e.  $s_{11} = 1.05 \times 10^{-2}$ ,  $s_{12} = -4.23 \times 10^{-3}$ ,  $s_{44} = 9.8 \times 10^{-3}$  (all in GPa<sup>-1</sup>). For the  $\gamma'$  precipitate the room temperature elastic constants for Ni<sub>3</sub>Al + Ta of Curwick [42] were extrapolated to 850°C assuming the same temperature dependence as for the elastic constants for pure nickel. This gave for the  $\gamma'$  material:

$$\begin{aligned}s_{11} &= 1.13 \times 10^{-2}; \\ s_{12} &= -4.5 \times 10^{-3}; \\ s_{44} &= 10.3 \times 10^{-3} \text{ (again all in GPa}^{-1}\text{).}\end{aligned}$$

The resulting difference between the elastic constants of the matrix and the precipitate were small, with the matrix being slightly stiffer than the precipitate.

Due to the symmetry of the microstructure, the upper and right boundaries were constrained to remain plane during the analysis. Nodes along the bottom and left boundaries were permitted to move only in the 1 and 2 directions, respectively. All FEM analyses were performed using an ABAQUS finite element code on a DG MV10 computer.

With this FEM model the thermal misfit stresses at 850°C were calculated throughout the  $\gamma$  matrix and the  $\gamma'$  particle. The distribution of the two scalar invariants of the local stresses: the negative pressure and the Mises effective stress are shown in Fig. 27(a), (b), and Fig. 28(a), (b), respectively for the  $\gamma$  and  $\gamma'$  components. In addition for the purpose of evaluation of the resolved shear stresses in the matrix and in the particle the actual tensor components of the stresses at three prominent nodal points (32, 44, and 148), in both the  $\gamma$  and the  $\gamma'$  materials are listed in Table 3. The positions of these nodes are shown in Fig. 26.

### 6.3. Finite element analysis of creep flow in the $\gamma/\gamma'$ microstructure

**6.3.1. The creep flow problem.** Since the TEM studies presented in Section 4 above, showed that the  $\gamma'$  precipitate remains undeformed until the very late stages of steady state creep, the precipitate was permitted to deform only elastically, while the matrix could deform both elastically and by creep. The <001> orientation is a multiple slip orientation. Therefore, no lattice rotations should occur in the course of creep deformation if all of the slip systems are active. Therefore, a simple power law relation was used to characterize the creep properties of the matrix, relating the equivalent strain rate  $\dot{\epsilon}_e$  to the equivalent stress  $\sigma_e$

$$\dot{\epsilon}_e = A\sigma_e^n. \quad (24)$$

The creep properties for Ni-6W [27] were used for the matrix in the analysis, with  $n = 4.8$  and the pre-exponential constant  $A$  was taken to be equal to  $5.4 \times 10^{-15}/\text{s MPa}^{4.8}$ . Clearly, this grossly underestimates the resistance of the  $\gamma$  matrix which has a very high Orowan resistance. This, however, is of

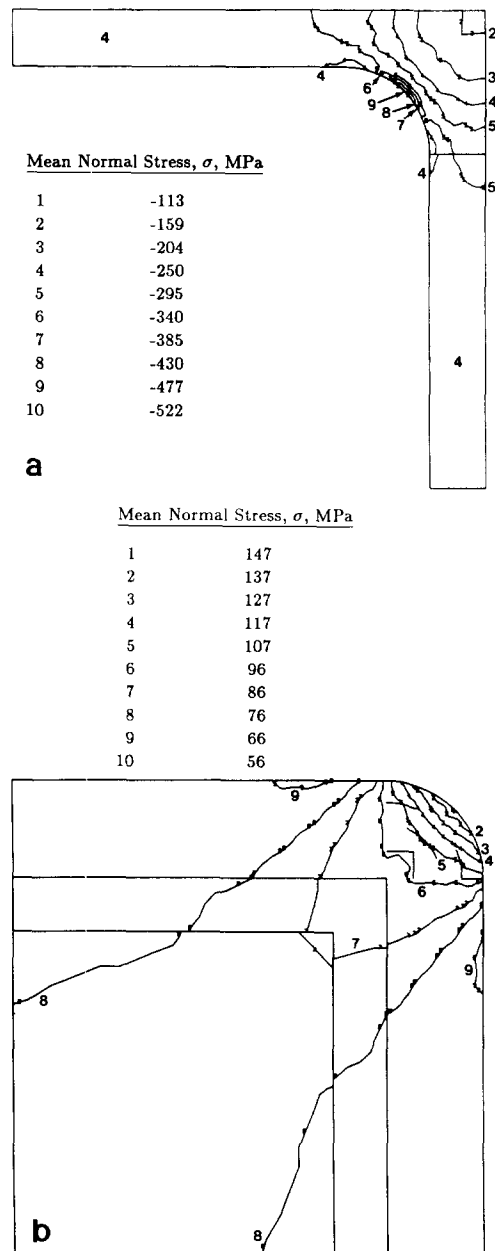


Fig. 27. The distribution of negative pressure (mean normal stress) associated with the initial misfit between the  $\gamma'$  particle and the surrounding  $\gamma$  matrix: (a) the  $\gamma$  matrix; (b) the  $\gamma'$  particle. (The solid lines indicate boundaries of mesh refinement.)

no consequence since the results can be scaled upward later.

Separate analyses were completed under conditions of imposed boundary displacement rate, and under constant loads applied to the upper boundary. For the case of imposed displacement rate analysis, the upper boundary was displaced with respect to the lower boundary to give a macroscopic tensile creep rate of  $2.5 \times 10^{-8}/\text{s}$ . Load control analyses were completed by imposing a constant load which was distributed along the upper boundary. All analysis was carried out at a temperature of 850°C.

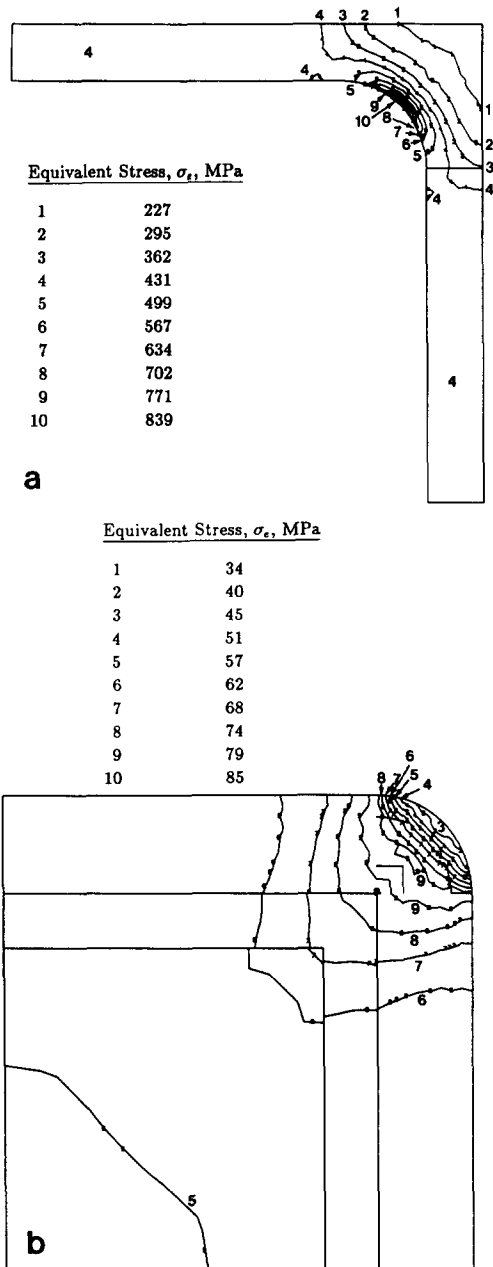


Fig. 28. The distribution of the Mises effective stress associated with the initial misfit between the  $\gamma'$  particle and the surrounding  $\gamma$  matrix: (a) the  $\gamma$  matrix; (b) the  $\gamma'$  particle. (The solid lines indicate boundaries of mesh refinement.)

**6.3.2. Creep at constant imposed displacement rate.** The initial thermal misfit stresses in the plane of the  $\gamma$  channels were compressive, while the stress normal to the channels was tensile. For the initial misfit of  $-3.05 \times 10^{-3}$  the stresses in the  $\gamma$  phase are rather high, with biaxial compressive stresses of 433 MPa in the plane of the channel, and a tensile stress of 50 MPa normal to the plane of the channel. In the generalized plane strain analysis, this gave equivalent misfit stresses of 456 MPa in the matrix material. These misfit stresses serve as a substantial additional

Table 3. Initial thermal misfit stresses at three selected nodes: 32, 44, and 148 in the  $\gamma/\gamma'$  microstructure ( $^{\circ}\text{C}$ )

$\sigma_1$ (MPa),	$\sigma_2$	$\sigma_3$	$\sigma_c$	$\sigma$
-433	50	-373	456	-252
49	-433	-373	456	-252
54	52	111	58	72

\*Locations of nodes 32, 44 and 148 are shown in Fig. 26.

driving force to the creep deformation process at the start of the analysis. (In a separate analysis, these stresses proved to be high enough to partially relax the misfit when the material was held at 850°C under no other imposed stresses or displacements. In that case the equivalent misfit stresses were reduced by 41% after a hold time of  $2.56 \times 10^6$  s.)

Displacing the upper boundary with respect to the lower at an average strain rate of  $2.5 \times 10^{-8}/\text{s}$  allowed for relaxation of misfit stresses in approximately  $1.54 \times 10^4$  s (4.28 h), during which equivalent creep strains of  $5.78 \times 10^{-3}$  accumulated in the matrix. As the creep progressed from this point on, there was a build-up of negative pressure in the horizontal channel and positive pressure in the vertical channel. These pressures built up monotonically from the corner of the precipitates to a maximum at the channel center, as shown in Fig. 29 at  $2.4 \times 10^5$  s. The corresponding equivalent stresses in the  $\gamma$  channels are shown in Fig. 30. The pressures continued to build up until the ratio of the maximum negative pressure to the equivalent stress reached a value of nearly 10 in the horizontal channel.

As the creep process proceeded, the material adjacent to the  $\gamma/\gamma'$  interface began to shear along the interface, showing a pattern of flow from the vertical channel toward the horizontal channel. This is shown in a plot of the distorted mesh in Fig. 31. Although

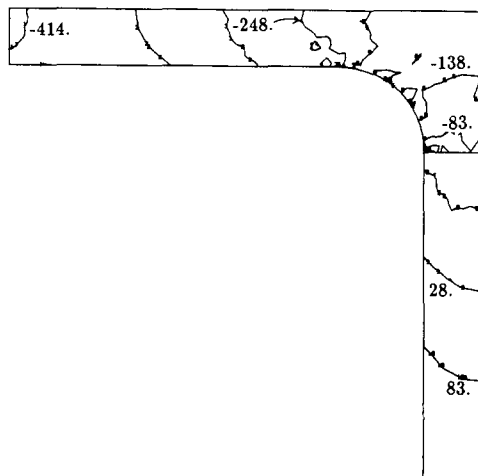


Fig. 29. The distribution of pressure in the  $\gamma$  channels in creep deformation at 850°C at an imposed average strain rate of  $2.5 \times 10^{-8}/\text{s}$ , after an elapsed time of  $2.4 \times 10^5$  s.

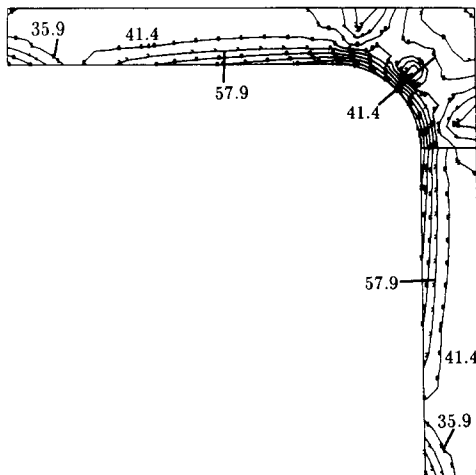


Fig. 30. The distribution of Mises equivalent stress in the  $\gamma$  channels in creep deformation under the same conditions given in the caption of Fig. 29.

the ratio of the maximum pressure to the equivalent stress remained roughly constant, there was a gradual increase in the matrix equivalent creep resistance, and therefore the absolute level of pressure rose gradually at very long times in the analysis. The volume average equivalent stresses in the matrix were 32, 35.6, and 40.8 MPa at times of  $1.75 \times 10^5$ ,  $2.07 \times 10^5$ , and  $2.41 \times 10^5$  s, respectively.

Since the  $\gamma'$  precipitate did not deform by creep, the stresses inside it continued to rise with increasing matrix creep deformation. In Fig. 32(a)–(c) the contours of equivalent stress are shown at times of  $1.1 \times 10^5$ ,  $4.3 \times 10^5$  and  $7.7 \times 10^5$  s. The maximum equivalent stresses at these times were 262, 965, and 1655 MPa, respectively. Compared to the experimentally measured value of the 0.2% yield strength at  $850^\circ\text{C}$ , these stresses were fairly low in the early stages of the analysis, but they exceed the initial yield stress of the two phase alloy at longer times. It was expected that at some critical point the precipitate would be sheared by dislocations as the stresses inside

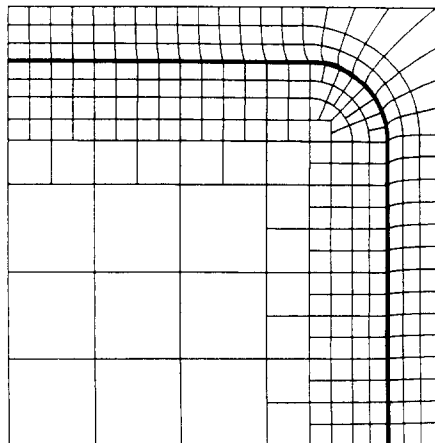


Fig. 31. Distorted finite element net due to creep flow in the  $\gamma$  phase channels.

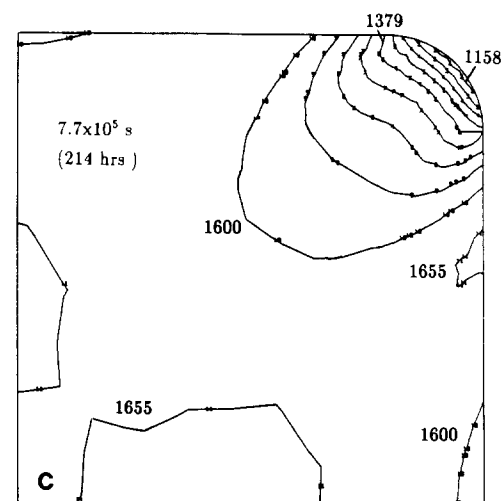
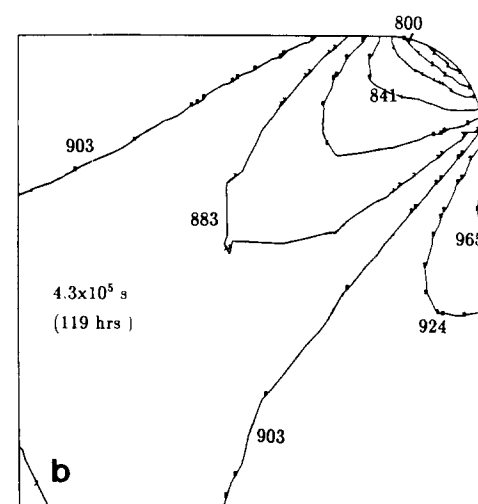
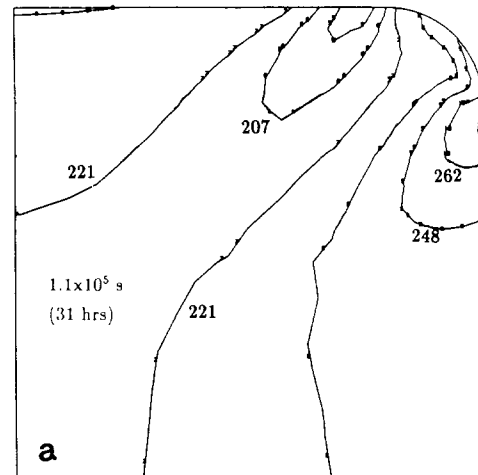


Fig. 32. The development of Mises effective stresses inside the  $\gamma'$  particles as the creep deformation progresses: (a) after  $1.1 \times 10^5$  s; (b) after  $4.3 \times 10^5$  s; (c) after  $7.7 \times 10^5$  s.

the precipitate rose to high enough levels, as was found to be the case experimentally at late stages of "steady state" creep.

*6.3.3. Creep under constant applied load.* With the same boundary conditions and material properties

as the imposed displacement rate analysis, several analyses were also performed with uniform tensile stresses applied to the upper boundary of the model. In these analyses, the macroscopic creep rate was calculated from the displacement rate of the upper boundary with respect to the lower.

Similar to the imposed displacement rate analysis, the application of a constant stress of 552 MPa gave an initial transient strain during which the misfit stresses were relaxed. This was followed by a gradual build-up of negative and positive pressure gradients in the horizontal and vertical channels, respectively as in the imposed displacement rate analysis. The precipitate was also increasingly stressed with accumulating creep strain in the matrix. However, the major difference between the applied displacement rate and applied load analyses was that for an applied stress of 552 MPa the relief of the misfit stresses and the development of the pressure gradients occurred in a shorter time [ $(P/\sigma_0)_{\text{max}} = 9.82$  at  $t = 1170$  s under constant applied load, compared to  $(P/\sigma_0)_{\text{max}} = 9.44$  at  $t = 1.38 \times 10^5$  s in the displacement rate control]. At long times ( $\approx 10^5$  s), the creep rate for the application of 552 MPa was about  $6.4 \times 10^{-7}$  /s which is much higher than the experimentally observed rate of  $2.5 \times 10^{-8}$  /s. This is another demonstration of the fact that the actual creep resistance of the two phase alloy is much higher than can be accounted for by a continuum approach utilizing bulk properties.

In summary, the FEM analysis has demonstrated the correctness of the analytical results of Schroeder and Webster presented in Section 6.1. The qualitative similarity of the two solutions which predict the build-up of important pressure gradients due to the creep flow of the  $\gamma$  "fluid" in the narrow channels between  $\gamma'$  precipitates is demonstrated in Fig. 33. Here the build-up of the negative pressure in the horizontal channel from the edges toward the center is plotted for the FEM analysis in comparison with the analysis of Schroeder and Webster. The results indicate that in the FEM analysis there is a finite increment above the S & W analysis. This difference is attributed to the material at the corners of the

precipitate that imposes additional constraints on the flow. This effect will be taken into account in Section 6.4 below in a modified S & W analysis.

It is necessary to point out here that the FEM analysis presented above which considered power-law bulk creep behavior for the matrix is not intended as a quantitatively accurate model for the real material as already stated above, but only as an exact but qualitatively instructive parallel. Thus, no importance should be attached to differences in the time constants between the model and the real material, which arise in part because in reality in the starting material the mobile dislocation density is orders of magnitude lower than the levels at steady state creep. This should give much lower effective creep rates and longer time constants until the dislocation density is built up to its steady state level (see also Haubensak and Argon [43]).

#### 6.4. Approximate dislocation mechanics analysis of channel flow in the $\gamma - \gamma'$ composite

As presented in Section 5 above, the plastic shear resistance of the  $\gamma$  channels is governed by an Orowan resistance  $\tau_{\text{or}}$ , a solid solution resistance,  $\tau_{\text{ss}}$ , and a dislocation resistance  $\tau_{\text{dis}}$ . Of these, the solid solution resistance is strain rate and temperature dependent, while the other two are not. Clearly, the high creep resistance of the CMSX-3 crystals in the  $\langle 001 \rangle$  orientation combines a high, and scale dependent deformation resistance of the  $\gamma$  channels with a substantial resistance that results from the build-up of pressure gradients due to the frictional drag of the non-deforming  $\gamma'$  particles. To combine these effects in an improved dislocation mechanics analysis we first define a total resolved shear resistance  $\tau_{\text{tot}}$  on the active octahedral slip planes as

$$\tau_{\text{tot}} = \tau_{\text{or}} + \tau_{\text{ss}} + \tau_{\text{dis}}. \quad (25)$$

As discussed in Section 5.4 at 850°C for a total tensile strain rate of  $2.5 \times 10^{-8}$  /s the solid solution resistance should be 17.5 MPa giving for  $\tau_{\text{tot}} = 194$  MPa (taking  $\tau_{\text{or}} = 166$  MPa, and  $\tau_{\text{dis}} = 10.5$  MPa). This gives a tensile deformation resistance  $\sigma_0 = 475$  MPa for the  $\gamma$  material in the  $\langle 001 \rangle$  orientation. Use of this resistance in equation (23) with  $R/t = L/(h\sqrt{\pi}) = 4.23$  would give a tensile creep resistance of 2.49 GPa which is now far in excess of the actual value of 552 MPa. This indicates that when the  $\gamma$  channels are populated by a knitted space network of dislocations of which a large fraction are lying along the  $\gamma/\gamma'$  interfaces, some sliding becomes possible along these interfaces as the  $\gamma$  phase deforms. This could occur by glide of the interface screw dislocations in the vertical channels and by a combination of glide and short range climb of the 60° mixed interface dislocations in the horizontal channels. We, therefore, need to consider a modification of equation (23) that incorporates deformation of thin plastic slabs in the presence of a wall friction coefficient  $\eta$ . Such a solution can be readily developed utilizing the

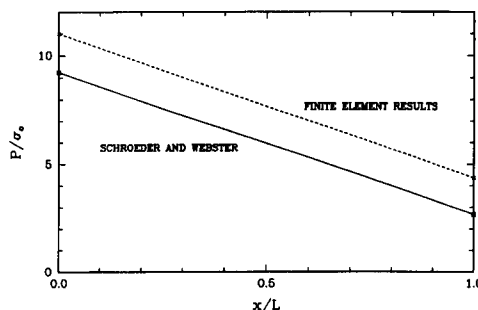


Fig. 33. The distribution of tensile tractions acting across the  $\gamma$  slab, calculated by the approximate model based on the analysis of Schroeder and Webster, and by the finite element method.

approach of Schroeder and Webster [39], which when adapted to the geometry of Fig. 25 gives the following expression for the average tensile stress  $P$ , where now account has also been taken of the corner material (see Appendix III)

$$\left(\frac{P}{\sigma_0}\right)_{\text{avg}}^{\text{tot}} = \frac{2[A(\sqrt{3}-1) + 2(h/L)]}{\sqrt{3}[1+(h/L)]^2} \quad (26)$$

where

$$A = (2/C^2)[\exp C - C - 1] \\ \therefore C = (2\eta L/h\sqrt{3}). \quad (27\text{a, b})$$

We now evaluate this expression for  $P = 552$  MPa,  $\sigma_0 = 475$  MPa, with  $L/(h\sqrt{3}) = 4.23$  as before, to determine the effective coefficient of wall friction  $\eta$  between the deforming  $\gamma$  "fluid", and the non-deforming elastic  $\gamma'$  particles. This gives an effective coefficient of friction of  $\eta = 0.112$  and an interface-average-shear-traction of  $\tau = 32.4$  MPa along the  $\gamma/\gamma'$  interface. This is considerably larger than the solid solution drag on screw dislocations and is no-doubt affected by the climb resistance of the  $60^\circ$  mixed dislocations along the  $\gamma/\gamma'$  interfaces of the horizontal  $\gamma$  channels as these dislocations are forced to displace along these interfaces during the flow of the  $\gamma$  "fluid".

In the absence of a more definitive treatment of this very complex problem, we consider this picture of the deformation of the  $\gamma$  matrix to be quite satisfactory.

### 6.5. The recovery resistance

As discussed in Section 5.8 the CMSX-3 crystals show very little recovery effects during rest periods of the order of  $10^4$  s at the test temperature of  $850^\circ\text{C}$ . This was verified also by *in situ* observations of dislocation structures characteristic of the "steady state" deformation range. Such three dimensionally knitted networks of dislocations showed negligible recovery effects in the TEM at  $850^\circ\text{C}$  for periods of observation of the order of 30 min. In samples previously crept to steady state, annealing at  $850^\circ\text{C}$  for 750 h, however, showed measurable reductions in dislocation density by factors of the order of 5. Reduction of the dislocation density by about a factor of 2 was also observed in *in situ* experiments at  $882^\circ\text{C}$  over periods of the order of  $4 \times 10^3$  s. This suggests that the recovery resistance of this material could in part be due to very sluggish diffusional transport in the  $\gamma$  phase. This was verified by a quantitative interpretation of the climb controlled shape changes of  $60^\circ$  mixed dislocations during the incubation phase. In the micrographs of these interrupted incubation experiments many cross glide events of screw dislocations in the  $\gamma$  channels were seen (see Fig. 10). When such a cross glide event occurs, a sharp  $90^\circ$  corner should be formed in both of the parallel  $60^\circ$  mixed dislocations that are part of the same long dipole loop laid out against opposing

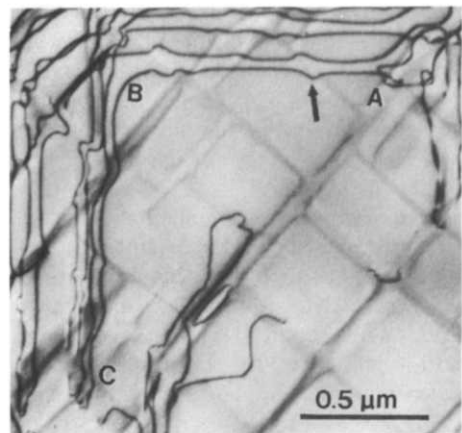


Fig. 34. Right angle turns due to cross glide in expanding prismatic loops in the  $\gamma$  channels. The rounding of the sharp corner at B resulting from diffusion controlled climb permits determination of an effective diffusion constant.

$\gamma/\gamma'$  interfaces. In the micrographs, however, these corners are seen considerably rounded as the enlargement in Fig. 34 shows. Such rounding is interpreted to be due to diffusion controlled climb of the  $60^\circ$  mixed dislocation in the plane of the interface under the action of the line tension, the applied climb force, and the mutual interaction force of the other arm of the elongated loop pressed against the opposite  $\gamma/\gamma'$  interface. This rounding by climb has occurred during a time interval  $\Delta t$  that the leading screw dislocation has taken to move from point B to C against the solid solution drag—which in this particular case is of the order of 100 s at  $825^\circ\text{C}$ . Defining an average climb distance  $\bar{\Delta}l$ , as the distance that the rounded arc at B in Fig. 34 sweeps out the area between the initial sharp corner and the final arc at B, an average climb velocity  $\bar{v}$  can be estimated as (Appendix 4)

$$\bar{v} = \frac{\bar{\Delta}l}{\Delta t} \approx 1.37 \times 10^{-8} \text{ cm/s.} \quad (28)$$

This gives a good estimate of the effective diffusion constant  $D_{\text{eff}}$  as [37]

$$D_{\text{eff}} = \frac{\bar{v}b_{\text{el}}^2 kT \ln(h/b)}{2\pi\Omega F_{\text{tot}}} \quad (29)$$

where  $b_{\text{el}} = b/\sqrt{2}$  is that edge component of the Burgers vector of the mixed dislocation that is involved in the climb motion,  $\Omega$  is the atomic volume, and  $F_{\text{tot}}$  is the total climb producing force, made up of the applied climb force, the line tension force and the interaction force. The latter is estimated to be  $(8.66 \times 10^{-3})\mu b$  (Appendix IV). (Parenthetically we note that while the rounding is rapid on the dislocation where the applied climb force is in the same direction as the line tension force, it is quite slow on the opposing pair of the dislocation where these two forces are in opposite directions.) Evaluation of equation (29) with the above values of the relevant quantities gives an effective diffusion

constant of  $D_{\text{eff}} = 3.1 \times 10^{-16} \text{ cm}^2/\text{s}$  at  $825^\circ\text{C}$ . For  $D_{\text{eff}} = D_0 \exp(-Q/RT)$  with the assumption that  $D_0$  is approximately  $1 \text{ cm}^2/\text{s}$ , the activation energy for this climb process is  $326 \text{ kJ/mol}$ . This is very close to the activation energy for diffusion of W in Ni and the activation energy for creep in Ni-W solid solutions [27].

For recovery involving annihilation of dislocations in the knitted network of dislocations in the  $\gamma$  channels diffusional transport distances can be expected to be between the channel thickness  $h$  and the channel length  $L$ . With an effective diffusion coefficient of  $6.9 \times 10^{-16} \text{ cm}^2/\text{s}$  at  $850^\circ\text{C}$ , the two bounds for the characteristic diffusion time  $t$  for recovery are

$$t_{\text{lb}} = h^2/D_{\text{eff}} = 5.2 \times 10^4 \text{ s} \quad (30\text{a})$$

$$t_{\text{ub}} = L^2/D_{\text{eff}} = 2.9 \times 10^6 \text{ s}. \quad (30\text{b})$$

From this we conclude that local rearrangement of dislocations in the three-dimensional network will occur on the scale of individual matrix channels, but at  $850^\circ\text{C}$  diffusion will be ineffective at promoting recovery of the networks on the larger scale of the precipitates. This is consistent with the results of the unloading recovery experiments, the *in situ* annealing experiments, and the bulk static annealing experiments reported in Section 3 above, and indicates that the recovery resistance is in part due to the presence of slow diffusing alloying elements in the matrix material, and in part due to the large diffusional transport distances governed by the distribution of the  $\gamma'$  precipitates.

## 7. DISCUSSION

Here we have given a quantitative account of the remarkable creep deformation resistance of a superalloy single crystal, CMSX-3, in the  $\langle 001 \rangle$  orientation. The principal distinguishing feature of this material is its high  $\gamma'$  phase content of the order of  $2/3$ , and the impenetrability of the  $\gamma'$  phase to the  $\gamma$  dislocations. Thus, in the range of  $\gamma'$  particle sizes of  $0.5 \mu\text{m}$  which tend to be relatively stable in the attractive creep regime of  $800\text{--}900^\circ\text{C}$ , the  $\gamma'$  acts as a rigid filler. This forces the topologically continuous  $\gamma$  phase to undergo complex patterns of creep flow during which quite significant mean normal stresses are developed in the  $\gamma$  phase that add to the deformation resistance. This latter aspect is particularly prevalent in the  $\langle 001 \rangle$  orientation. In other orientations such as  $\langle 011 \rangle$  or  $\langle 111 \rangle$  where the creep flow does not require the development of mean normal stresses to the same degree as in the  $\langle 001 \rangle$  orientation, the uniaxial creep resistances of the crystals are considerably lower [43].

In accounting for the apparent steady state creep resistance of our material no account was taken of any recovery in resistances. This was for two reasons. First, the principal Orowan resistance and

the secondary solid solution resistance is not subject to alteration by recovery of dislocation structures. They should be unaffected as long as the dimensions of the  $\gamma'$  precipitates and the thicknesses of the  $\gamma$  phase channels remain unaltered. The dislocation resistance that is subject to a recovery effect was found to be of relatively minor importance. A second and perhaps a more major reason for the relative stability of the knitted three dimensional dislocation networks in the  $\gamma$  phase channels was found to be due to a very low effective diffusion constant which at  $825^\circ\text{C}$  was estimated to be  $3.1 \times 10^{-16} \text{ cm}^2/\text{s}$ . Such a low diffusion constant is no doubt a result of the many alloying elements in the  $\gamma$  phase (see Table 1) which must affect diffusional transport of matter by binding of vacancies to solute atoms not only in the lattice, but perhaps even more effectively along the dislocation cores.

The lack of agreement between the experimentally measured activation energies for creep and activation energies for diffusion are further evidence that while diffusional processes may alter local dislocation arrangements, they do not directly govern the overall creep resistance and rate of accumulation of creep deformation. A thorough accounting of the time-dependent build-up of local internal stresses and their influence on dislocation motion would be necessary for a complete description of the creep curve. It is interesting to note here that in the creep regime which we have reported on here the ordered  $\gamma'$  phase does not deform before the late tertiary stages of creep when the mounting internal stresses become very large. Therefore, the alloy does not exhibit any unusual positive temperature dependence of the creep resistance characteristic of the flow stress for the pure  $\gamma'$  phase [44]. That this is so was demonstrated in Section 3 where we have indicated that conventional approaches to determining activation energy for creep by considering the changes in minimum creep rate with increasing temperature at constant stress were operationally successful and led to positive (albeit quite large) activation energies. Outside of the creep regime, at higher strain rates (and higher stresses), it is well known that the  $\gamma'$  particles are sheared. In that regime the temperature dependence of the flow stress should again return to be positive—in keeping with expectations.

The creep behavior of the CMSX-3 type high  $\gamma'$  content crystals is relatively free of transients. The principal primary transient was shown to be due to the relaxation of the initial thermal misfit stresses and unrelated to recovery or work hardening. This is consistent with experimental observations, and is another reason for the recovery resistance of the alloy, since elimination of the knitted dislocation network would require the re-establishment of the internal stresses of misfit. This is because a significant fraction of the knitted network dislocations are evidently “polarized” and act as misfit neutralizing interface dislocations.

The FEM model has demonstrated that even though the matrix may have a means of exhibiting steady state creep, this condition is never attained during the deformation of the heterogeneous alloy. Under either imposed constant strain rates or constant applied stresses the internal stresses continue to rise monotonically. A consequence of this is that while the  $\gamma'$  phase is initially impenetrable by  $\gamma$  dislocations, the latter eventually can penetrate the  $\gamma'$  particles when the threshold stresses for entry are reached. This is observed in the TEM micrographs and is interpreted to be a contributing factor to the eventual tertiary acceleration of creep rate.

## 8. CONCLUSIONS

1. In the temperature range of 800–900°C and stress ranges of interest in creep, the  $\gamma'$  precipitates are dislocation-free and are undeformable until the very late stages of tertiary creep, after several percent of creep deformation has accumulated.

2. Incubation periods prior to the onset of primary creep are present in virgin crystals due to the difficulty of spreading dislocations through the narrow  $\gamma$  channels from widely spaced sources of grown-in dislocations.

3. Dislocations move through the material by bowing out through the narrow matrix channels of the  $\gamma$  phase on {111} planes.

4. In the early stages of primary creep, locally all dislocations have the same Burgers vector indicating their origin at a common source. As the creep process continues, dislocations with different Burgers vectors interpenetrate into the individual matrix channels and begin to form a knitted space network.

5. Steady state creep is characterized by a three-dimensional knitted nodal network, which contains multiple Burgers vectors. The network fills the matrix material, and diffusion controlled static recovery is ineffective at causing rearrangements in it at temperatures of 850°C or less. For this reason, a stress dependent dynamic recovery mechanism appears to be responsible for maintaining the creep process.

6. The principal cause of the high creep resistance of the CMSX-3 crystals is the non-deformability of the  $\gamma'$  particles forcing the  $\gamma$  phase to undergo complex flow patterns in narrow channels.

7. Nearly one quarter of the deformation resistance is due to the mean normal stresses that develop during the creep flow of the  $\gamma$  phase in the narrow channels between the “rigid”  $\gamma'$  particles.

8. A true steady state is not possible in the deformation of the  $\gamma/\gamma'$  microstructure, since the internal stresses due to “channel flow” rise monotonically during creep.

9. A consequence of the rise of the internal stresses is the eventual penetration of  $\gamma$  dislocations into the  $\gamma'$  precipitates. Shearing of the  $\gamma'$  precipitates by

individual  $\gamma$  dislocations will occur frequently when the local internal stresses reach a level of  $\chi_{APB}/b$ .

10. The primary transient following the incubation stage of deformation is due to the relief of the initial thermal misfit stresses between the  $\gamma$  and  $\gamma'$  phases, and is unrelated to any work hardening or recovery process.

11. The three-dimensional dislocation networks in the  $\gamma$  phase channels characteristic of the creeping material serve to neutralize the misfit stresses and are very resistant to recovery. This is in part because of the presence of slow diffusing alloying elements in the matrix material, aggravated by the long diffusional transport distances, prescribed by the regular arrangement of the  $\gamma'$  precipitates, and in part due to the fact that the knitted network of dislocations in the  $\gamma$  channels acts as a misfit neutralizing interface dislocation network.

*Acknowledgements*—This research was supported by NSF/MRL under Grant DMR 87-19217 through the center for Materials Science and Engineering at MIT and by an IBM doctoral fellowship to TMP during the terminal year of this research. The authors would like to express their appreciation to Dr Mehmet Doner of the Allison Gas Turbine Division of General Motors for the generous donation of all the single crystals used in this research, and to Mr F. Haubensak for his assistance in the analysis of the effective diffusion constant. Moreover, they gratefully acknowledge the help of Professor D. M. Parks and Dr E. Zywicki in the FEM analysis.

## REFERENCES

1. G. R. Leverant and B. H. Kear, *Metall. Trans.* **1A**, 491 (1970).
2. G. R. Leverant, B. H. Kear and J. M. Oblak, *Metall. Trans.* **4A**, 355 (1973).
3. P. Caron and T. Khan, *Mater. Sci. Engng* **61**, 173 (1983).
4. M. V. Nathal and L. J. Ebert, *Metall. Trans.* **16A**, 427 (1985).
5. M. V. Nathal and L. J. Ebert, *Metall. Trans.* **16A**, 1863 (1985).
6. R. A. MacKay and L. J. Ebert, *Metall. Trans.* **16A**, 1969 (1985).
7. C. Carry and J. L. Strudel, *Acta metall.* **26**, 859 (1978).
8. B. H. Kear and J. M. Oblak, *J. Physique* **12**, 7 (1974).
9. A. A. Hopgood and J. W. Martin, *Mater. Sci. Engng* **82**, 27 (1986).
10. G. A. Webster and B. J. Pearcey, *Metal Sci. J.* **1**, 97 (1967).
11. R. A. MacKay and L. J. Ebert, *Scripta metall.* **17**, 1217 (1983).
12. I-W. Chen and A. S. Argon, *Acta metall.* **29**, 1321 (1981).
13. A. S. Argon, A. K. Bhattacharya and T. M. Pollock, in *Constitutive Relations and their Physical Basis* (edited by S. I. Andersen *et al.*), p. 39. Risø National Laboratory, Roskilde, Denmark (1987).
14. T. M. Pollock and A. S. Argon, in *Superalloys 1988* (edited by D. Duhl *et al.*), p. 285. The Metall. Soc., Warrendale, Pa (1988).
15. T. M. Pollock and A. S. Argon, in *Proc. Fourth Int. Conf. on Creep and Fracture of Engineering Materials and Structures* (edited by B. Wilshire), p. 287. Inst. of Metals, London (1990).

16. P. Caron, Y. Ohta, Y. G. Nakagawa and T. Khan, in *Superalloys 1988* (edited by D. Duhl *et al.*), p. 215. The Metall. Soc., Warrendale, Pa (1988).
17. A. Fredholm and J. L. Strudel, *Superalloys 1984*, p. 211. The Metall. Soc. A.I.M.E., Philadelphia, Pa (1984).
18. M. V. Nathal, R. A. MacKay and R. V. Miner, *Metall. Trans.* **20A**, 133 (1989).
19. M. Feller-Kniepmeier and T. Link, *Mater. Sci. Engng A113*, 191 (1989).
20. T. P. Gabb, S. L. Draper, D. R. Hull, R. A. MacKay and M. V. Nathal, *Mater. Sci. Engng A118*, 59 (1989).
21. F. Prinz, A. S. Argon and W. C. Moffatt, *Acta metall.* **30**, 821 (1982).
22. M. V. Nathal, R. A. MacKay and R. G. Garlick, *Mater. Sci. Engng* **75**, 195 (1985).
23. D. A. Grose and G. S. Ansell, *Metall. Trans.* **12A**, 1631 (1981).
24. A. F. Giamei, D. D. Pearson and D. L. Anton, *Proc. MRS Symp. on High Temperature Ordered Intermetallic Alloys*, Vol. 39, p. 293 (1985).
25. T. M. Pollock, Ph.D. thesis, MIT, Cambridge, Mass. (1989).
26. U. F. Kocks, A. S. Argon and M. F. Ashby, *Progress in Materials Science* (edited by B. Chalmers *et al.*), Vol. 19. Pergamon Press, Oxford (1975).
27. W. R. Johnson, C. R. Barrett and W. D. Nix, *Metall. Trans.* **3A**, 963 (1972).
28. P. A. Flinn, *Trans. Am. Inst. Min. Engrs* **218**, 145 (1960).
29. M. V. Nathal, J. O. Diaz and R. V. Miner, in *Proc. MRS Symp.*, Vol. 133, p. 269. MRS, Pittsburgh, Pa (1988).
30. E. Nembach and G. Neite, *Prog. Mater. Sci.* **29**, 277 (1985).
31. Y. Q. Sun and P. M. Hazzledine, *Phil. Mag.* **A58**, 603 (1988).
32. Y. Lin, T. Takasugi, O. Izumi and H. Ohta, *Phil. Mag.* **A58**, 81 (1988).
33. A. Veld, G. Boom, P. Bronsveld and J. DeHosson, *Scripta metall.* **19**, 105 (1985).
34. M. Dollar and I. Bernstein, in *Superalloys 1988* (edited by D. Duhl *et al.*), p. 275. The Metall. Soc., Warrendale, Pa (1988).
35. J. Douin, P. Veyssiére and P. Beauchamp, *Phil. Mag.* **A54**, 375 (1986).
36. P. Caron and T. Khan, *Phil. Mag.* **A57**, 859 (1988).
37. J. P. Hirth and J. Lothe, *Theory of Dislocations*, 2nd edn. Wiley Interscience, New York (1982).
38. S. M. Copley and B. H. Kear, *Trans. Am. Inst. Min. Engrs* **239**, 984 (1967).
39. W. Schroeder and D. A. Webster, *J. appl. Mech.* **16**, 289 (1949).
40. G. Simmons and H. Wang, *Single Crystal Elastic Constants and Calculated Aggregate Properties*. M.I.T. Press, Cambridge, Mass. (1971).
41. M. Doner, private communication, Allison Gas Turbine Division of General Motors.
42. L. Curwick, Ph.D. thesis, Univ. of Minnesota, Minneapolis, Minn. (1972).
43. F. Haubensak and A. S. Argon. To be published.
44. T. Khan, P. Caron and S. Naka, in *High Temperature Aluminides and Intermetallics* (edited by S. H. Wheng *et al.*), p. 219. The Metall. Soc., Warrendale, Pa (1990).

## APPENDIX I

### *The Solid Solution Resistance*

Consider a solid-solution-drag-controlled-velocity expression for dislocations

$$v = v_0 \exp\left(-\frac{Q - (\tau - \tau_0)V^*}{kT}\right) \quad (\text{AI.1})$$

where the individual terms are as defined in Section 5.4. The resolved shear stress  $\tau$  that drives the dislocations includes in addition to the applied stress the misfit stresses due to differences in lattice parameter between the  $\gamma$  and  $\gamma'$  phases and the further modification of these due to thermal expansion. As discussed in Section 5.4, available evidence suggests that the misfit is negligible at room temperature and increases monotonically with increasing temperature. In a finite element study of the stresses due to misfit (as well as the continuing creep process in the  $\gamma$  matrix) [25], it was established that at 850°C the biaxial misfit stresses  $\sigma_{11}$  and  $\sigma_{22}$  at the center of the  $\gamma'$  particle face are compressive, while the stress  $\sigma_{33}$  acting across the thin  $\gamma$  slab is tensile and have the magnitudes of

$$\sigma_{11} = \sigma_{22} = -433 \text{ MPa} \quad (\text{AI.2})$$

$$\sigma_{33} = 50 \text{ MPa}. \quad (\text{AI.3})$$

The study also gave the variations in these stresses from the center of the  $\gamma$  slab to the borders where they are 30% lower. Nevertheless, a volume average of the individual stress components over the representative  $\gamma$  slab gives a reduction of only 4% when compared with the values of these stresses at the center of the  $\gamma'$  face.

In the analysis that has been discussed in Section 5.4 only the stresses in the  $\gamma$  channels normal to the applied tensile stress are considered since these will govern the initial creep rate.

As discussed in Section 5.2 the typical Orowan resistance of the  $\gamma$  channels is 166 MPa. Since the misfit stresses were considered zero at room temperature and differing  $\gamma$  and  $\gamma'$  coefficients of thermal expansion give the values in equations (AI.2) and (AI.3) at 850°C, the values at other temperatures were obtained by linear interpolation. Furthermore, the Schmid factor for all principal stresses in the directions 1, 2, and 3 when resolved on the  $\{111\}\langle110\rangle$  slip system is  $1/\sqrt{6}$ . With these considerations it is easy to calculate the total resolved shear stresses driving the dislocations in the horizontal  $\gamma$  channels to obtain the values given in Table 2.

## APPENDIX II

### *Penetration of Dislocations into $\gamma'$ Particles*

Under conventional expectations the penetration of dislocations into the  $\gamma'$  phase should occur in the form of a superdislocation where the  $\gamma$  dislocations enter the  $\gamma'$  particle in a configuration sketched out in Fig. 23(a) and (b). The free energy difference of the bulged superdislocation configuration of Fig. 23(b) in comparison with the energy of the two  $\gamma$  dislocations of Fig. 23(a) is

$$\Delta G = 2R\theta\epsilon_{sd} - A\epsilon_{2d} - 2\tau b\Delta A \quad (\text{AII.1})$$

where

$$A = 2R \sin \theta \quad (\text{AII.2a})$$

$$\Delta A = R^2(\theta - \sin \theta \cos \theta) \quad (\text{AII.2b})$$

$$R = \epsilon_{sd}/2bt \quad (\text{AII.2c})$$

where  $\epsilon_{sd}$  is the line energy of the superdislocation of either 60° mixed type or screw type. In equation (AII.1) the first two terms represent the line energy difference between the bowed out superdislocation with energy  $\epsilon_{sd}$  and radius of curvature  $R$  and the line energies,  $\epsilon_{2d}$ , of the pair of straight  $\gamma$  phase dislocations that the superdislocation of length  $A$  is replacing. The last term in equation (AII.1) is the work done by the resolved shear stress  $\tau$  during the formation of the superdislocation bulge nucleus. Making the substitutions indicated in equations (AII.2a–c), using a small angle  $\theta$  bow-

out expansion, and obtaining the extremum configuration of the bulge from the usual condition

$$\left( \frac{\partial \Delta G}{\partial A} \right)_r = 0 \quad (\text{AII.3})$$

gives the activation free energy  $\Delta G^*$  of the saddle point configuration as

$$\Delta G^* = (\epsilon_{sd} - \epsilon_{2d}) A^* - \tau b (A^*)^3 / b \epsilon_{sd} \quad (\text{AII.4a})$$

$$A^* = [2\epsilon_{sd}(\epsilon_{sd} - \epsilon_{2d})]^{1/2} / (\tau b). \quad (\text{AII.4b})$$

And finally substitution of (AII.4b) into (AII.4a) gives

$$\Delta G^* = [2\epsilon_{sd}(\epsilon_{sd} - \epsilon_{2d})]^{3/2} / 3\epsilon_{sd} \tau b. \quad (\text{AII.5})$$

The line energies of the mixed superdislocation  $\epsilon_{sdm}$ , the screw superdislocation  $\epsilon_{sds}$ , and the energies of the corresponding pairs  $\epsilon_{2dm}$ , and  $\epsilon_{2ds}$  of  $\gamma$  phase dislocations pressed against the  $\gamma'$  interface by the resolved shear stress  $\tau$  for entry from the horizontal channels or vertical channels can again be obtained readily by elementary methods. They are

$$\begin{aligned} \epsilon_{sdm} &= \frac{\mu b^2}{\pi(1-v)} \left[ \left( \frac{4-v}{4} \right) \ln \left( \frac{\alpha R}{b} \right) \right. \\ &\quad \left. - \left( \frac{4-v}{8} \right) \ln \left( \frac{\alpha \Delta_m}{eb} \right) - \frac{1}{12} \ln \left( \frac{\alpha \delta_m}{eb} \right) \right] \end{aligned} \quad (\text{AII.6a})$$

$$\Delta_m = \frac{\mu b^2}{2\pi(1-v)\chi_{APB}} \left( \frac{4-v}{4} \right) \quad (\text{AII.6b})$$

$$\begin{aligned} \epsilon_{2dm} &= \frac{\mu b^2}{\pi(1-v)} \left[ \left( \frac{4-v}{4} \right) \ln \left( \frac{\alpha R}{b} \right) \right. \\ &\quad \left. - \left( \frac{4-v}{8} \right) \ln \left( \frac{\alpha \zeta_m}{b} \right) - \frac{1}{12} \ln \left( \frac{\alpha \delta_m}{eb} \right) \right] \end{aligned} \quad (\text{AII.7a})$$

$$\zeta_m = \frac{\mu b}{2\pi(1-v)} \left( \frac{4-v}{4} \right) \frac{1}{\tau} \quad (\text{AII.7b})$$

$$\begin{aligned} \epsilon_{2ds} &= \frac{\mu b^2}{\pi} \left[ \ln \left( \frac{\alpha R}{b} \right) - \frac{1}{2} \ln \left( \frac{\alpha \Delta_s}{eb} \right) \right. \\ &\quad \left. - \frac{1}{12} \left( \frac{2-3v}{1-v} \right) \ln \left( \frac{\alpha \delta_s}{eb} \right) \right] \end{aligned} \quad (\text{AII.8a})$$

$$\Delta_s = \frac{\mu b^2}{2\pi\chi_{APB}} \quad (\text{AII.8b})$$

$$\begin{aligned} \epsilon_{2ds} &= \frac{\mu b^2}{\pi} \left[ \ln \left( \frac{\alpha R}{b} \right) - \frac{1}{2} \ln \left( \frac{\alpha \zeta_s}{b} \right) \right. \\ &\quad \left. - \frac{1}{12} \left( \frac{2-3v}{1-v} \right) \ln \left( \frac{\alpha \delta_s}{eb} \right) \right] \end{aligned} \quad (\text{AII.9a})$$

$$\zeta_s = \frac{\mu b}{2\pi\tau}. \quad (\text{AII.9b})$$

The above line energies have all been obtained on the assumption that the antiphase boundary (APB) widths,  $\Delta_m$  and  $\Delta_s$ , are much larger than the corresponding stacking fault (SF) widths  $\delta_m$  and  $\delta_s$  in the related extended mixed dislocations and extended screw dislocations respectively, so that when the width of the APBs are considered no significant alterations occur in the SF widths. This appears to be warranted since in the TEM pictures extended dislocations are rarely resolved while observations of separation between the full dislocations in superdislocations is often observed in Ni<sub>3</sub>Al [32]. In the above equations  $\zeta_m$  and  $\zeta_s$  are the separations between the pairs of  $\gamma$  dislocations pressed together by the resolved shear stress  $\tau$  where the lead dislocation, in turn, presses against the  $\gamma'$  particle boundary.

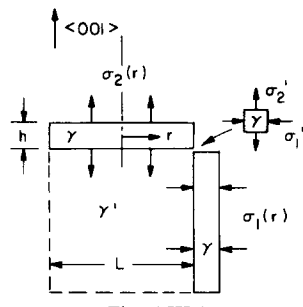


Fig. AIII.1

Substitution of the energies in equations (AII.6–9) into equation (AII.5) gives the expressions for the activation energies  $\Delta G_m^*$  and  $\Delta G_s^*$  of equations (15a–c) and (16a–c).

### APPENDIX III

#### Channel Flow Resistance in the Presence of Slippage

An important contribution to the resistance of creep flow of the  $\gamma$  material in the narrow channels comes from the flow in the horizontal and vertical channels shown in Fig. AIII.1. The relevant friction-hill problem in these channels in the presence of wall friction, having an effective coefficient of friction  $\eta$ , has been solved by Schroeder and Webster [39]. To adapt their solution to the problem in the  $\gamma/\gamma'$  microstructure we need to consider the corner material to be in a state of pure shear as shown in Fig. AIII.1, subjected to stresses  $\sigma'_1$  and  $\sigma'_2$  that are numerically equal. For this element to be at the state of flow the magnitude of the effective stress  $\sigma'_0$  due to the stresses  $\sigma'_1$  and  $\sigma'_2$  must be

$$\sigma'_0 = \sigma_0 / \sqrt{3}. \quad (\text{AIII.1})$$

Integration of the basic differential equation (AIII.2) [39] for the local traction  $\sigma_2(r)$  on the faces of the horizontal slab between the end point  $r = R$  where

$$\sigma_2 = \sigma_0 (\sqrt{3} - 1) / \sqrt{3},$$

and  $r = r$ , where  $\sigma_2 = \sigma_2(r)$ , gives

$$\frac{d\sigma_2}{\sigma_2} = -\frac{2\eta}{h} dr \quad (\text{AIII.2})$$

$$\sigma_2(r) = \sigma_0 \frac{(\sqrt{3} - 1)}{\sqrt{3}} \left[ \exp \left( \frac{2\eta}{h} (R - r) \right) \right]. \quad (\text{AIII.3})$$

Integration of (AIII.3) over the entire face of the slab to obtain the average traction  $\bar{\sigma}_2$  on the slab (excluding the corner material) gives for the latter

$$\begin{aligned} \bar{\sigma}_2 &= \sigma_0 \frac{(\sqrt{3} - 1)}{\sqrt{3}} \frac{2}{C^2} [\exp(C) - C - 1] \\ &= \frac{\sigma_0 (\sqrt{3} - 1)}{\sqrt{3}} A \end{aligned} \quad (\text{AIII.4})$$

where

$$C = 2\eta R/h. \quad (\text{AIII.5})$$

Replacing  $C$  with  $2\eta L/h\sqrt{\pi}$ , as before, to generalize the circular disk result to the square disk of the  $\gamma'$  particle face, and including the tractions  $\sigma'_1$  and  $\sigma'_2$  on the faces of the corner material into total average traction  $\bar{\sigma}_2$ , one obtains readily for the latter

$$\bar{\sigma}_2 = \frac{\sigma_0}{(1 + h/L)^2} \left[ \frac{\bar{\sigma}_2'}{\sigma_0} + \frac{2}{\sqrt{3}} \frac{h}{L} \right]. \quad (\text{AIII.6})$$

Finally, considering that the compressive tractions on the vertical slab are numerically the same as those in equation (AIII.6), and that to make the transverse direction stress free, these tractions must be removed by adding a negative pressure by this amount gives for the total average vertical tractions  $P$  on the horizontal slab

$$\frac{P}{\sigma_0} = \frac{2}{\sqrt{3}(1+h/L)^2} [A(\sqrt{3}-1) + 2h/L] \quad (\text{AIII.7})$$

where  $A$  was defined in equation (AIII.4) above.

## APPENDIX IV

### *Diffusional Rounding by Climb of Sharp Corner Produced by Cross Glide*

There are three forces that act on the  $60^\circ$  mixed dislocation tending to round out, by diffusional climb, the sharp corner produced by cross glide of the leading screw dislocation from one glide plane into another, resulting in the final geometry shown in Fig. AIV.1(a). These forces are the *interaction force*  $F_{\text{int}}$ , in the climb direction between the two dislocations pressed against the opposing  $\gamma/\gamma'$  interfaces; the *applied climb force*  $F_a$ ; and the *line tension force*  $F_h$ . They are, (considered as acting on the lower dislocation in Fig. AIV. 1(a), toward the center of curvature)

$$F_{\text{int}} = -\frac{\mu}{2\pi\sqrt{3/2}h} [(0.577b_s^2 + 1.32b_{e1}^2/(1-\nu) - 0.192b_{e2}^2/(1-\nu)] \quad (\text{AIV.1})$$

$$F_{\text{int}} = -\frac{(0.992)}{2\pi\sqrt{3/2}} \left(\frac{b}{h}\right) \mu b \quad (\text{AIV.2})$$

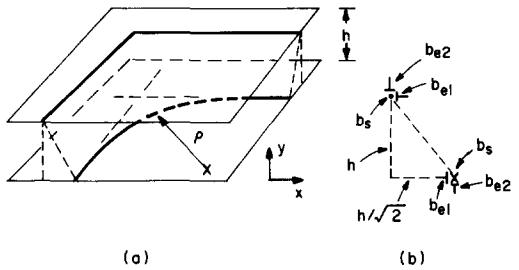


Fig. AIV.1 (a) and (b).

where the Burgers vectors of the component dislocations  $b_s$ ,  $b_{e1}$ ,  $b_{e2}$  are shown in Fig. AIV 1(b). Furthermore

$$F_a = (\sigma/\mu)(b_{e1}/b)\mu b \quad (\text{AIV.3})$$

and

$$F_h = [(b/(4\pi\rho))\ln(h/b)]\mu b \quad (\text{AIV.4})$$

where  $\rho$  is the current radius of curvature of the corner. For the radius of curvature  $\rho$  shown in Fig. 34 ( $\rho = 0.1 \mu\text{m}$ )

$$F_{\text{tot}} = F_a + F_{\text{int}} + F_h \approx (8.66 \times 10^{-3})\mu b. \quad (\text{AIV.5})$$

Substitution of this total force into the climb equation for the dislocation line gives the effective diffusion constant  $D_{\text{eff}}$

$$D_{\text{eff}} = \frac{\bar{v}b_{e1}^2 kT \ln(h/b)}{2\pi\Omega F_{\text{tot}}} \quad (\text{AIV.6})$$

Taking the relevant values as

$$\mu = 48.2 \text{ GPa}$$

$$b = 2.54 \text{ \AA}$$

$$b_{e1} = b/\sqrt{2}$$

$$\bar{v} = \Delta l/\Delta t \approx 1.37 \times 10^{-8} \text{ cm/s}$$

$$T = 1098 \text{ K}$$

$$\Omega = 1.16 \times 10^{-23} \text{ cm}^3$$

we find that  $D_{\text{eff}} = 3.1 \times 10^{-16} \text{ cm}^2/\text{s}$  at  $825^\circ\text{C}$ .